Pergamon

Int. J. Solids Structures Vol. 31, No. 12/13, pp. 1695–1736, 1994
Elsevier Science Ltd
Printed in Great Britain
0020-7683/94 $7.00 + .00

0020-7683(93)E0014-9

ANALYSES OF METAL FORMING PROBLEMS BY THE BOUNDARY ELEMENT METHOD

ABHIJIT CHANDRA
Department of Aerospace and Mechanical Engineering, The University of Arizona, Tucson, AZ 85721, U.S.A.

Abstract—Forming is one of the most common manufacturing processes. This paper reviews the applications of the boundary element method (BEM) to analyses of various forming processes, e.g. extrusion, rolling, profile rolling, etc.

The boundary element formulations for elastic–plastic and elastic–viscoplastic problems involving large strains and rotations are considered first. The elastic strains are assumed to remain small. The rotations and nonelastic strains, however, are allowed to be large. Bulk compressibility effects, which are often ignored for finite strain problems of metallic solids, are explicitly included here.

An updated Lagrangian approach is adopted for the BEM analyses of forming processes. The frictional conditions at the tool–workpiece interface are introduced through a smeared interface element. For several forming problems, the frictional stresses change direction at the neutral region, and the location of this region is not known *a priori*. It is demonstrated here that the BEM can be used to efficiently and accurately analyse this class of planar and axisymmetric forming problems involving both material and geometric nonlinearities, along with complicated interface conditions. The numerical results obtained from the BEM analyses are also compared to those obtained from FEM with regard to efficiency and accuracy.

1. INTRODUCTION

Metal forming processes such as extrusion, rolling, sheet metal forming, etc., generally subject the workpiece to finite strains and displacements. The components of elastic strain in these examples are generally limited to about 10^{-3} since the elastic moduli of metals are typically about three orders of magnitude larger than the yield stress. Thus, the nonelastic strain components, which can be of the order of unity, greatly dominate the elastic strains.

A considerable body of literature (e.g. McMeeking and Rice, 1975; Lee *et al.*, 1977; Dawson and Thompson, 1977; Oh *et al.*, 1983; Onate and Zienkiewicz, 1983; Chandra and Mukherjee, 1984b, c) exists where the finite element method has been used to analyse metal forming problems using rigid-plastic, elastic–plastic, flow-type, and elastic–viscoplastic material models. While the finite element method has been very successful in several engineering applications, it is quite sensitive to aspect ratios of individual elements. This requires remeshing where severe deformation is involved. Moreover, the secondary variables obtained through numerical differentiation in a finite element technique are inherently less accurate than the primary variables. In a typical displacement formulation, the secondary variables are stresses and, in a problem involving both material and geometric nonlinearities, the stresses at the present time essentially drive the problem through future time steps. These are the two major limitations of typical FEM approaches that stand in the way of robust and cost effective, yet accurate, FEM analyses of metal forming processes. The analyses of Onate and Zienkiewicz (1983), Dawson (1984), and Kobayashi *et al.* (1989) are cost effective, but all of them treat the metal forming process as viscous flow. Thus, very critical quantities like residual stresses are difficult to recover from such analyses. Also, the viscous flow approaches are more suitable for steady-state processes.

Rolling is a very common metal working process in industry. In view of the tremendous amount and wide variety of rolled products manufactured every year, it can also be considered as one of the most important ones. For more than half a century, numerous investigations, both analytical and experimental, have been carried out on rolling. The slab method based on a simplified equilibrium of force was first suggested by von Kármán (1925). Orowan (1943) and Hill (1959) among others, derived approximate solutions of the equilibrium equations by using various assumptions. In later years, slip-line (Alexander,

1972; among others) and upper bound (Avitzur, 1980; among others) methods were introduced to rolling analysis.

The slab, slip-line, and upper bound methods have been widely used in theoretical analyses of metal forming in general and have gained popularity in industrial design of rolling mills. However, owing to the complexities of deformation involved in metal forming processes, particularly in rolling, various degrees of simplifications and idealizations have become necessary. Accordingly, the methods cited above have provided useful but limited information on metal deformation in rolling.

Over the last decade, several attempts have been made to solve the rolling problem by using the finite element method (Dawson and Thompson, 1977; Li and Kobayashi, 1982; Mori *et al.*, 1982; Oh *et al.*, 1983 and Dawson, 1987; to mention a few). Dawson models the rolling problem as viscous flow. Li and Kobayashi and Mori *et al.* solve the plane-strain rolling problem using a rigid-plastic finite element method based on the infinitesimal theory of plastic deformation.

For rolling, forging and ring compression problems, the boundary conditions are typically not well known at the tool–workpiece interfaces. A unique feature of deformation in ring compression (also in rolling and forging) is the existence of a neutral point (or region) along the tool–workpiece interface, where the tangential relative velocity between the deforming material and the die becomes zero. The frictional stresses change direction at the neutral point (or region). The location of this point (or region), however, is not known *a priori*. In ring compression, when a short ring is compressed between two flat, parallel plates, the inner surface bulges in the same or opposite direction of the outer surface, depending on the friction conditions at the interface. The inner surface bulges outward if the friction is low and bulges inward if the friction is high. Because the change in internal diameter of the compressed ring is sensitive to friction at the tool–workpiece interface, and due to the simple geometry, ring compression is widely used to evaluate the effects of interfacial friction conditions in various metal working processes.

In order to determine the effects quantitatively, however, the relationship between the geometrical change of the workpiece and the friction condition at the interface must be established. This apsect of ring compression has been investigated by various researchers. Avitzur (1969) and Lee and Altan (1972) used upper bound solutions, and Chen and Kobayashi (1978) developed a variational formulation for finite element analysis of ring compression using a rigid-plastic material model.

Forming processes are also being used increasingly in manufacturing profiled work-pieces. Some of the well-known advantages of profile forming over metal cutting are a shorter production period, reduced raw material requirements, and a more favorable fibrous and strain-hardened structure of the processed material. Among the different types of forming processes used to manufacture tooth-profiled workpieces, rolling has attained the broadest range of applications in the manufacturing industry. One of the most important applications of profile rolling is in gear manufacturing and cold rolling of involute profiles. It is a very effective and efficient way of manufacturing gears (Lange and Kurz, 1984). However, the profile rolling process, conceived and developed in the factory, has not been investigated adequately. As a result, even today, the design of the profile rolling process is mostly empirical.

The boundary element method (BEM—also called the boundary integral equation method) is rooted in classical integral equation formulations of boundary value problems, such as the work of famous mathematicians like Fredholm and Volterra. As is described in other papers in this issue, it is a "natural" approach for linear problems in that many linear partial differential operators can be transformed into equivalent integral forms through the use of appropriate Green's functions. It is not surprising to observe, therefore, that the principal BEM applications in computational solid mechanics in the 1960s primarily dealt with linear problems such as torsion of elastic bars (Jaswon and Ponter, 1963), bending of elastic plates (Jaswon and Maiti, 1968), or classical elastostatics (Cruse, 1969, 1974; Rizzo, 1967). The method was carried forward during the 1970s to include problems with material nonlinearities such as plasticity (e.g. Swedlow and Cruse, 1971; Mendelson, 1973; Riccardella, 1973; Banerjee and Cathie, 1980; Banerjee and Butterfield, 1981; Doblare *et*

al., 1982) or viscoplasticity (e.g. Chaudonneret, 1977, 1980; Mukherjee, 1982; Telles and Brebbia, 1983). Recently, the BEM has been applied to fully nonlinear problems, including both material and geometrical nonlinearities (e.g. Chandra and Mukherjee, 1983, 1984a; Mukherjee and Chandra, 1984, 1987; Okada *et al.*, 1987).

The BEM is another general purpose method. It is far more tolerant of aspect ratio degradation than is the FEM and can yield secondary variables as accurate as the primary ones (Banerjee and Butterfield, 1981; Mukherjee, 1982; Chandra and Mukherjee, 1983, 1984a). Due to these advantages, BEM has been used recently to analyse the stress and deformation fields in complicated metal forming problems involving both material and geometric nonlinearities, as well as frictional interface conditions. Chandra and Mukherjee (1985, 1987) analysed plane-strain extrusion and sheet metal forming problems. Chandra and Saigal (1991) analysed axisymmetric extrusion problems. Chandra (1989) used a BEM formulation to investigate the stress and deformation histories of profile rolling of gears. For profile rolling, the rolling contact boundary condition is simulated by translating a displacement distribution corresponding to a modified Hertzian pressure distribution (Bhargava *et al.*, 1985). This pressure distribution is used to estimate the effects of inelasticity on the contact width and the continuity of the tool–workpiece interface. Using the BEM, Chandra (1989) investigated the slab rolling process and Chandra and Srivastava (1991) investigated the axisymmetric ring compression problem. Both of these problems involve neutral zones whose positions are not known *a priori*. The BEM, being essentially a mixed formulation, is found to be very suitable for handling such interface conditions.

A treatise of the applications of the BEM to this class of metal forming problems involving complicated interface conditions, in addition to material and geometric nonlinearities, is the main purpose of this paper. It starts with a review of the BEM formulations for elastic–plastic and elastic–viscoplastic problems involving large strains and rotations. The BEM formulations are capable of using any of a class of combined creep-plasticity constitutive models (e.g. Hart, 1976, 1982; Anand, 1982) with state variables for the descriptions of material behavior. Applications of the BEM formulations to several metal forming problems, such as planar and axisymmetric extrusion problems, slab rolling problems, axisymmetric ring compression problems, and profile rolling problems, are considered next. Particular attention is paid to the interface conditions for these forming processes. The detailed stress and deformation histories obtained by the BEM are presented, and the insights gained from them are discussed. These insights can be very useful for designing effective and efficient metal forming processes.

2. THE BOUNDARY ELEMENT FORMULATIONS FOR PROBLEMS WITH MATERIAL AND GEOMETRICAL NONLINEARITIES

This section is devoted to a discussion of solutions of large strain–large rotation problems in the presence of plasticity or viscoplasticity using the boundary element method. For metal forming processes, the components of elastic strain are generally limited to about 10^{-3} since the elastic moduli of metals are typically about three orders of magnitude larger than the yield stress. Thus, the nonelastic strain components, which can be of the order of unity, greatly dominate the elastic strains. Accordingly, it is assumed throughout that the elastic strains are infinitesimal while the nonelastic strains, as well as the rotations, can be arbitrary. The formulation presented here is based on an updated Lagrangian approach in which the configuration of a body of time t is used as reference for the deformation between t and $t+\Delta t$. This necessitates updating of the geometry during computer simulation of deformation, but provides great simplifications in the BEM formulation.

2.1. *Kinematics*

A three-dimensional body is considered. Unless otherwise indicated, the range of indices is 1, 2, 3. Referring to a set of spatially fixed rectangular Cartesian coordinates, a material particle in the body in a reference configuration is assumed to have coordinates X_i. The same particle has coordinates x_i in the current configuration.

The displacement vector $\mathbf{u}_i$ can be defined as

$$\mathbf{u}_i = x_i - X_i. \tag{1}$$

The velocity of this material point during deformation is denoted by v_i. The deformation rate d_{ij} is the symmetric part of the velocity gradient,

$$d_{ij} = \frac{1}{2}\left[\frac{\partial v_i}{\partial x_j} + \frac{\partial v_j}{\partial x_i}\right], \tag{2}$$

whereas the spin

$$\omega_{ij} = \frac{1}{2}\left[\frac{\partial v_i}{\partial x_j} - \frac{\partial v_j}{\partial x_i}\right]. \tag{3}$$

The deformation gradient $\mathbf{F}$ is given as

$$\mathbf{F} = \frac{\partial \mathbf{x}}{\partial \mathbf{X}} = \mathbf{R} \cdot \mathbf{U}, \tag{4}$$

where $\mathbf{R}$ is the rotation tensor and $\mathbf{U}$ is the deformation tensor. From an alternative perspective, we can also view the displacement field $\mathbf{u}$ as a combination of rotation $\mathbf{R}$ and deformation $\mathbf{U}$. In many previous analyses, the spin ω was considered to be the rate of rotation. However, as shown by several researchers (Atluri, 1984; William, 1984; Chandra and Mukherjee, 1986a), that assumption can lead to spurious oscillations in stresses if high shearing strain is involved. In many forming operations, such as extrusion, the shearing strain remains quite small. However, for other forming processes, e.g. profile rolling, high shear strains can occur in a localized region. For such cases, the procedures using the Jaumann rate can lead to spurious oscillations. In the present work, rotation rate Ω is defined as:

$$\Omega = \omega - \tfrac{1}{2}\mathbf{R} \cdot [\dot{\mathbf{U}} \cdot \mathbf{U}^{-1} - \mathbf{U}^{-1} \cdot \dot{\mathbf{U}}] \cdot \mathbf{R}^T \tag{5}$$

(Atluri, 1984; Chandra and Mukherjee, 1986a), where $\mathbf{R}^T$ is the transpose of $\mathbf{R}$. Here, Ω is considered to be the rotation rate of a material element; thus, it also represents the rotation rate of the material coordinate frame—a set of coordinates attached to the material element.

2.2. *Constitutive assumptions*

The BEM formulation presented next is valid for a wide range of elastic–viscoplastic models. It is valid for compressible as well as incompressible plasticity.

The first assumption is that the deformation rate tensor can be linearly decomposed into an elastic and a nonelastic part (Nemat-Nasser, 1982; Chandra and Mukherjee, 1986a):

$$d_{ij} = d_{ij}^{(e)} + d_{ij}^{(n)}. \tag{6}$$

The next step, relating $\mathbf{d}^{(e)}$ to the stress, is very important. Assuming that the elastic field obeys hypoelasticity, we can write

$$\overset{\square}{\sigma} = \phi(\mathbf{d}^{(e)}) = \lambda(\operatorname{tr} \mathbf{d}^{(e)})\mathbf{I} + 2G\mathbf{d}^{(e)}, \tag{7a}$$

or, in component form,

$$\overset{\square}{\sigma}_{ij} = \lambda d_{kk}^{(e)} \delta_{ij} + 2G d_{ij}^{(e)}. \tag{7b}$$

Here, λ and G are Lamé constants, $\overset{\square}{\sigma}$ is an, as yet, unspecified but objective rate of the stress, and $\mathbf{d}^{(e)}$ is the elastic part of the deformation rate tensor.

The proposal here is to proceed from $\phi(\mathbf{d}^{(e)})$ to the Cauchy stress in a desired globally fixed basis by using the equation

$$\sigma(t) = \mathbf{R}(t)\sigma_0\mathbf{R}^T(t) + \mathbf{R}(t)\left[\int_0^t \mathbf{R}^T(\tau)\phi(\mathbf{d}^{(e)})\mathbf{R}(\tau)\,\mathrm{d}\tau\right]\mathbf{R}^T(t). \tag{8}$$

The value of the Cauchy stress at time zero is given by σ_0. The symbols in the above equation are matrices corresponding to the appropriate tensors.

The rationale behind this proposal is to observe that the expression $\mathbf{R}^T\phi(\mathbf{d}^{(e)})\mathbf{R}$ delivers the components of $\phi(\mathbf{d}^{(e)})$ in a local basis that is rotating with respect to the fixed global basis, with $\mathbf{R}$ as the measure of this rotation. Integration is then carried out with respect to an observer in the rotating basis (or with respect to the material coordinate frame). Finally, premultiplication by $\mathbf{R}$ and postmultiplication by $\mathbf{R}^T$, at any time, delivers the Cauchy stress components in the desired global basis. As shown by Chandra and Mukherjee (1986a), in view of eqns (7)–(8), $\overset{\square}{\sigma}$ is equivalent to the Dienes rate of Cauchy stress (Dienes, 1979; also called the Green–Naghdi rate by Johnson and Bamman, 1984). Goddard and Miller (1966) also present an equation similar to (8) for the inverse of the Jaumann derivative. Rolph and Bathe (1984) consider a special situation when the direction of principal stretches remains fixed in the body during deformation. Equations (7)–(8) are also found to be equivalent to those obtained by Rolph and Bathe for this particular situation.

Dafalias (1984) and Aifantis (1984) proposed decomposing the rotation tensor $\mathbf{R}$ into an elastic rotation $\mathbf{R}^{(e)}$ and a nonelastic rotation $\mathbf{R}^{(n)}$. However, the research to obtain physical forms of $\mathbf{R}^{(e)}$ and $\mathbf{R}^{(n)}$ is still at an early stage. In the present work, the elastic field is assumed to be governed by hypoelasticity, and eqn (8) with the total rotation tensor is used for obtaining Cauchy stress in a desired global, spatially fixed basis.

The mathematical structure of the nonelastic material models with state variables that are of interest to this study can be summarized by the following equations (Hart, 1976, 1982; Mukherjee, 1982; Chandra and Mukherjee, 1986a):

$$d_{ij}^{(n)} = f_{ij}[\sigma_{ij}, q_{ij}^{(k)}], \tag{9}$$

$$\overset{\square}{q}_{ij}^{(k)} = g_{ij}^{(k)}[\sigma_{ij}, q_{ij}^{(l)}]. \tag{10}$$

They state that the history dependence of $d_{ij}^{(n)}$ at any time can be represented by the current value of the stress and suitably chosen state variables q_{ij}, which can be scalars of tensors. For incompressible nonelastic deformation,

$$d_{kk}^{(n)} = 0. \tag{11}$$

Equations (9)–(11) are valid for uniform temperature, so thermal strains and temperature effects are neglected. In the interest of brevity, further discussions of these equations are avoided here. A more detailed discussion of the small strain model can be found in Mukherjee (1982).

The particular model used for planar problems is that due to Hart (1976, 1982) generalized to the case of large strains and rotations (Chandra and Mukherjee, 1984a, 1986a; Chandra, 1989). Material response in dilatation is assumed to be elastic. The model has two state variables: the anelastic strain $\varepsilon_{ij}^{(a)}$, a stored strain that reflects the magnitude and direction of prior deformation history and is responsible for induced anisotropy; and a scalar state variable H, the hardness, which is analogous to an isotropic strain-hardening variable or current yield stress. The evolution of $\varepsilon_{ij}^{(a)}$ can be expressed as:

$$\overset{\square}{\varepsilon}_{ij}^{(a)} = d_{ij}^{(n)} - d_{ij}^{(p)}, \tag{12}$$

where $d_{ij}^{(p)}$ represents the completely irrecoverable (permanent) path-dependent deformation rate. Since $\varepsilon_{ij}^{(a)}$ is a proper state variable, its objective rate is used in eqn (12), and $\varepsilon_{ij}^{(a)}$ is

obtained in a spatially fixed reference frame by integrating $\overset{\square}{\varepsilon}{}^{(a)}_{ij}$ in the same manner as for $\overset{\square}{\sigma}_{ij}$.

For axisymmetric ring compression and axisymmetric extrusion analyses, the material model due to Anand (1982) using a single state variable representing current hardness is used. For cases involving relatively small shear strains (less than unity), the rotation rate Ω_{ij} can be assumed to be the same as the spin tensor ω_{ij}. For such cases, the hypoelastic law can also be written in terms of the Jaumann rate of the Cauchy stress as

$$\overset{*}{\sigma}_{ij} \lambda d^{(e)}_{kk} \delta_{ij} + 2G d^{(e)}_{ij}, \tag{13}$$

when

$$\overset{*}{\sigma}_{ij} = \dot{\sigma}_{ij} + \sigma_{ik}\omega_{kj} - \omega_{ik}\sigma_{kj} \tag{14}$$

and

$$\dot{\sigma}_{ij} = \frac{\partial \sigma_{ij}}{\partial t} + \frac{\partial \sigma_{ij}}{\partial x_k} v_k. \tag{15}$$

2.3. *BEM formulation for velocities*

A BEM formulation for large strain–large rotation elastic–plastic and elastic–visco-plastic problems can now be obtained by utilizing an appropriate form of Betti's reciprocal theorem (Chandra and Mukherjee, 1983, 1984a). Alternatively, a weighted residual approach in an updated Lagrangian frame can be pursued (Okada *et al.*, 1987). Such an approach uses a rate-of-equilibrium equation in terms of the material rate of the Lagrange stress, and the weighting function is chosen to be the displacement field of fundamental solutions for the small strain elastic problems. These two approaches yield exactly equivalent final expressions.

Starting from an appropriate form of Betti's reciprocal theorem (Chandra and Mukherjee, 1983, 1984a; Chandra, 1989), we can write

$$\int_B \overset{\square}{\sigma}_{ij} \varepsilon^{(R)}_{ij} \, \mathrm{d}V = \int_B \sigma^{(R)}_{ij} d^{(e)}_{ij} \, \mathrm{d}V, \tag{16}$$

where the reference solution denoted by a superscript (R) is the fundamental solution for small strain elasticity problems. The integrands on either side of eqn (16) are identical by virtue of the hypoelasticity eqn (7). Also, it should be noted that the domain of integration of eqn (16) is the current volume.

Equation (16) must next be written in terms of the known reference domain B^0. Use of the updated Lagrangian frame renders this procedure particularly simple. A consequence of this assumption during each small step is that, since the current configuration at the start of the step is also the reference configuration, the deformation gradient $\mathbf{F}$ in eqn (4) is approximately equal to the identity tensor $\mathbf{I}$. Also, $\mathbf{R} \cong \mathbf{U} \cong \mathbf{I}$. Hence, $\Omega \cong \omega$ in an updated Lagrangian frame. As will be shown later, the choice of an updated Lagrangian frame significantly simplifies various relationships, particularly the one between the material rate of the Lagrange (or nominal) stress S and the Jaumann or corotational rate of the Cauchy stress σ.

In expressing eqn (16) in terms of the reference configuration, the next step requires the determination of the objective rates of the Kirchhoff stress and of the Cauchy stress. Starting from the equation

$$J\boldsymbol{\sigma} = \boldsymbol{\tau}, \tag{17}$$

where $J = \det(\mathbf{F})$ (det denotes determinant), differentiating eqn (17), and noting that

$$\dot{J} = J \operatorname{tr}(\mathbf{D}) \tag{18}$$

(where tr denotes trace), it is easy to show that

$$\dot{\boldsymbol{\tau}} = J[\operatorname{tr}(\mathbf{D})\boldsymbol{\sigma} + \dot{\boldsymbol{\sigma}}]. \tag{19}$$

In the updated Lagrangian approach, $J \cong 1$ and $\boldsymbol{\sigma} \cong \boldsymbol{\tau}$. Thus, using (18) and the definition of the particular objective rate (Chandra and Mukherjee, 1986a, b) with respect to an observer rotating with the material particle, one easily obtains

$$\overset{\square}{\boldsymbol{\sigma}} = \overset{\square}{\boldsymbol{\tau}} - \operatorname{tr}(\mathbf{D})\boldsymbol{\sigma} \tag{20}$$

or, in component form,

$$\overset{\square}{\sigma}_{ij} = \overset{\square}{\tau}_{ij} - v_{k,k}\sigma_{ij}. \tag{21}$$

It should also be noted that

$$d_{kk} = -\frac{\dot{\rho}}{\rho}, \tag{22}$$

where ρ is the current density at a material point. Thus, if the deformation is incompressible, this term can be ignored and $\overset{\square}{\sigma}_{ij}$ is set equal to $\overset{\square}{\tau}_{ij}$. This is usually done for metal deformation with infinitesimal elastic and finite nonelastic strains, since the nonelastic portion of metal deformation is often volume preserving. Such, however, is not the case for compressible materials, and eqn (21) must be used explicitly.

For compressible materials, we get (Chandra and Mukherjee, 1986b)

$$\overset{\square}{\sigma}_{ij} = \overset{\square}{\tau}_{ij} - v_{k,k}\sigma_{ij} - k_b v_{k,k}\delta_{ij}, \tag{23}$$

where k_b is the bulk compressibility coefficient. For metal forming applications, the compressibility effects may be neglected. It is then more convenient to recast the above equation in the form

$$\overset{\square}{\sigma}_{ij} = \overset{\square}{\tau}_{ij} + C_{ijkl}v_{k,l}, \tag{24}$$

where

$$C_{ijkl} = -\sigma_{ij}\delta_{kl}. \tag{25}$$

The rate of equilibrium equation in terms of the material rate of the Lagrange (nonsymmetric, nominal) stress in the absence of body forces is given as

$$\dot{s}_{ji,j} = 0. \tag{26}$$

Strictly speaking, the derivative of the rate of Lagrange stress should be taken with respect to reference coordinates X_j, but here, in the updated Lagrangian frame, these derivatives are approximately the same as those with respect to x_j. Also, in the updated Lagrangian frame,

$$d_{ij} = \dot{E}_{ij}, \tag{27}$$

where $\dot{E}_{ij}$ is the material rate of the Green–Saint Venant strain.

The next step requires the relationship between the Jaumann rate of the Kirchoff stress and the material rate of the Lagrange stress. Starting from

$$\boldsymbol{\tau} = \mathbf{F} \cdot \mathbf{s}, \tag{28}$$

one differentiates this equation with respect to time and the definition of the objective rate to get

$$\overset{\square}{\boldsymbol{\tau}} - \boldsymbol{\tau} \cdot \boldsymbol{\Omega} + \boldsymbol{\Omega} \cdot \boldsymbol{\tau} = \dot{\mathbf{F}} \cdot \boldsymbol{\tau} \cdot \mathbf{F}^{-1} + \mathbf{F} \cdot \dot{\mathbf{s}} \tag{29}$$

so that

$$\dot{\mathbf{s}} = \mathbf{F}^{-1} \cdot (\overset{\square}{\boldsymbol{\tau}} - \boldsymbol{\tau} \cdot \boldsymbol{\Omega} + \boldsymbol{\Omega} \cdot \boldsymbol{\tau}) - \mathbf{F}^{-1} \cdot \dot{\mathbf{F}} \cdot \boldsymbol{\tau} \cdot \mathbf{F}^{-1}. \tag{30}$$

This complicated expression simplifies immensely in the updated Lagrangian frame. One gets:

$$\dot{\mathbf{s}} = \overset{\square}{\boldsymbol{\tau}} - \boldsymbol{\tau} \cdot \boldsymbol{\Omega} + \boldsymbol{\Omega} \cdot \boldsymbol{\tau} - \dot{\mathbf{F}} \cdot \boldsymbol{\tau}. \tag{31}$$

In the updated Lagrangian frame, $\mathbf{F} \cong \mathbf{R} \cong \mathbf{U} = \mathbf{I}$ and $\dot{\mathbf{F}} = \mathbf{L}$. Accordingly, in eqn (5), $\boldsymbol{\Omega} \cong \boldsymbol{\omega}$. Thus, at the beginning of each step, after updating of the previous reference configuration is completed, we can write (in updated Lagrangian frame)

$$\dot{\mathbf{s}} = \overset{\square}{\boldsymbol{\tau}} - \boldsymbol{\tau} \cdot \boldsymbol{\omega} + \boldsymbol{\omega} \cdot \boldsymbol{\tau} - \mathbf{L} \cdot \boldsymbol{\tau}. \tag{32}$$

Since

$$\mathbf{L} = \mathbf{D} + \boldsymbol{\omega} = \frac{\partial \mathbf{V}}{\partial \mathbf{x}}, \tag{33}$$

is in component form, we get

$$\dot{s}_{ji} = \overset{\square}{\tau}_j - \sigma_{jk}\omega_{ki} - d_{jk}\sigma_{ki}. \tag{34}$$

Again, it is convenient to write this equation in the form

$$\overset{\square}{\tau}_{ji} = \dot{s}_{ji} + G_{jikl} v_{k,l}, \tag{35}$$

where

$$2G_{ijkl} = \sigma_{ik}\delta_{jl} + \sigma_{jl}\delta_{ik} + \sigma_{jk}\delta_{li} - \sigma_{li}\delta_{jk}.$$

The tensor G_{ijkl} is, therefore, a function only of the components of the Cauchy stress σ_{ij}. Using the convention

$$\{v_{k,l}\}^T = [v_{1,1} v_{2,1} v_{3,1} v_{1,2} v_{2,2} v_{3,2} v_{1,3} v_{2,3} v_{3,3}], \tag{36}$$

the matrix corresponding to G_{ijkl} is

$[G] =$

$$\begin{bmatrix}
\sigma_{11} & & & & & & & & \\
\sigma_{12} & -\tfrac{1}{2}(\sigma_{11}-\sigma_{22}) & & & & \text{(Symmetric)} & & & \\
\sigma_{13} & \tfrac{1}{2}\sigma_{23} & -\tfrac{1}{2}(\sigma_{11}-\sigma_{33}) & & & & & & \\
0 & \tfrac{1}{2}(\sigma_{11}+\sigma_{22}) & \tfrac{1}{2}\sigma_{23} & -\tfrac{1}{2}(\sigma_{22}-\sigma_{11}) & & & & & \\
0 & 0 & 0 & \sigma_{12} & \sigma_{22} & & & & \\
0 & \tfrac{1}{2}\sigma_{13} & -\tfrac{1}{2}\sigma_{12} & \tfrac{1}{2}\sigma_{13} & \sigma_{23} & -\tfrac{1}{2}(\sigma_{22}-\sigma_{33}) & & & \\
0 & \tfrac{1}{2}\sigma_{23} & \tfrac{1}{2}(\sigma_{11}+\sigma_{33}) & -\tfrac{1}{2}\sigma_{23} & 0 & \tfrac{1}{2}\sigma_{12} & -\tfrac{1}{2}(\sigma_{33}-\sigma_{11}) & & \\
0 & -\tfrac{1}{2}\sigma_{13} & \tfrac{1}{2}\sigma_{12} & \tfrac{1}{2}\sigma_{13} & 0 & \tfrac{1}{2}(\sigma_{22}+\sigma_{33}) & \tfrac{1}{2}\sigma_{12} & -\tfrac{1}{2}(\sigma_{33}-\sigma_{22}) & \\
0 & 0 & 0 & 0 & 0 & 0 & \sigma_{13} & \sigma_{23} & \sigma_{33}
\end{bmatrix}.$$

The form of eqn (16) in the reference configuration B^0 now becomes

$$\int_{B^0} (\dot{s}_{ji} + G_{jikl} v_{k,l} + C_{jikl} v_{k,l}) \varepsilon_{ij}^{(R)} \, \mathrm{d}V = \int_{B^0} \sigma_{ij}^{(R)} \dot{E}_{ij}^{(e)} \, \mathrm{d}V. \tag{37}$$

The rest of the derivation parallels that of the small-deformation situation. Using the equilibrium, the law of hypoelasticity, and the divergence theorem, the left-hand side of eqn (37) becomes

$$\text{L.H.S.} = e_j \left[\int_{\partial B^0} U_{ij} \dot{s}_{kl} n_k^0 \, \mathrm{d}s^0 + \int_{B^0} U_{ij,m} G_{mikl} v_{k,l} \, \mathrm{d}V^0 + \int_{B^0} U_{ij,m} C_{mikl} v_{k,l} \, \mathrm{d}V^0 \right]. \tag{38}$$

Similarly, the right-hand side of eqn (37) becomes

$$\text{R.H.S.} = e_j \left[\int_{\partial B^0} T_{ij} v_i \, \mathrm{d}s^0 + \int_{B^0} \Delta(p, q) \delta_{ij} v_i \, \mathrm{d}V^0 - \int_{B^0} [\lambda U_{ij,l} d_{kk}^{(n)} + 2G U_{ij,k} d_{ik}^{(n)}] \, \mathrm{d}V^0 \right]. \tag{39}$$

Finally, equating the expressions in eqns (38) and (39) and using the relevant property of the Dirac delta function, one obtains the equation

$$\begin{aligned}
v_j(p) = & \int_{\partial B^0} [U_{ij}(p, Q) \dot{\tau}_i(Q) - T_{ij}(p, Q) v_i(Q)] \, \mathrm{d}S_Q^0 \\
& + \int_{B^0} \left[\lambda U_{ij,i}(p, q) d_{kk}^{(n)}(q) + 2G U_{ij,k}(p, q) d_{ik}^{(n)}(q) \right] \mathrm{d}V_q^0 \\
& + \int_{B^0} U_{ij,m}(p, q) G_{mikl}(q) v_{k,l}(q) \, \mathrm{d}V_q^0 \\
& + \int_{B^0} U_{ij,m}(p, q) C_{mikl}(q) v_{k,l}(q) \, \mathrm{d}V_q^0,
\end{aligned} \tag{40}$$

where $\dot{\tau}_i = n_j^0 \dot{s}_{ji}$.

Comparing eqn (40) with the corresponding equation for small strains (Mukherjee, 1982), it is seen that the first two integrals on the right-hand side of the above equation are analogous to the small-strain elastic–viscoplastic formulation. The traction rate term $\dot{\tau}_i$ requires special care and is discussed later. The third term is the so-called "geometric correction" term that arises due to finite deformations and rotations inside the body. The last integral is a consequence of bulk compressibility. If incompressible metal deformation is being studied, this last integral vanishes altogether, and so does the term containing $d_{kk}^{(n)}$ in the second integral of eqn (40).

Using eqn (34), the traction rate $\dot{\tau}_i$ in eqn (40) can be written as

$$\dot{\tau}_i = n_j \dot{s}_{ji} = \dot{t}_i - n_j \sigma_{jk} \omega_{ki} - n_j d_{jk} \sigma_{ki} = \dot{t}_i - n_j G_{jikl} v_{k,l}, \tag{41}$$

where

$$\dot{t}_i = n_j \overset{\square}{\tau}_{ji} = n_j \overset{\square}{\sigma}_{ji} - n_j C_{jikl} v_{k,l}. \tag{42}$$

The presence of the G tensor in the boundary traction expression is sometimes referred to as "load correction" and is a consequence, during deformation, of the change in the area of a surface element and the rotation of the unit normal at a point on it. The rate $\dot{t}_i$ can be interpreted as a component of the rate of the prescribed follower force, per unit deformed surface area, on the deforming boundary.

It can be seen that, unlike elastic–viscoplastic problems with small strains and rotations, the unknown velocity gradient now occurs in the surface as well as in some of the domain integrals in eqn (40). Thus, iterations now become necessary at each time step. This has been carried out in order to obtain the numerical results presented later in this paper.

As before, the limit $p \to P$ is taken so that eqn (40) becomes

$$\begin{aligned} C_{ij}(P) v_i(P) = & \int_{\partial B^0} [U_{ij}(P, Q) \dot{\tau}_i(Q) - T_{ij}(P, Q) v_i(Q)] \, \mathrm{d}S_Q^0 \\ & + \int_{B^0} [\lambda U_{ij,j}(P, q) d_{kk}^{(n)}(q) + 2G U_{ij,k}(P, q) d_{ik}^{(n)}(q)] \, \mathrm{d}V_q^0 \\ & + \int_{B^0} U_{ij,m}(P, q) G_{mikl}(q) v_{k,l}(q) \, \mathrm{d}V_Q^0 \\ & + \int_{\partial B^0} U_{ij,m}(P, q) \bar{C}_{mikl}(q) v_{k,l}(q) \, \mathrm{d}V_Q^0. \end{aligned} \tag{43}$$

The coefficient C_{ij} is the same as in the case of small strain–small rotation problems (Banerjee and Butterfield, 1981, Mukherjee, 1982).

2.4. *Internal stress rates*

As mentioned above, analytical differentiation of eqn (40) at a source point is the best way to obtain velocity rates at internal points. To this end, a differentiated version of eqn (40) is

$$\begin{aligned} v_{j,I}(p) = & \int_{\partial B^0} [U_{ij,I}(p, Q) \dot{\tau}_i(Q) - T_{ij,I}(p, Q) v_i(Q)] \, \mathrm{d}S_Q^0 \\ & + \frac{\partial}{\partial x_I} \int_{B^0} [\lambda U_{ij,i}(p, q) d_{kk}^{(n)}(q) + 2G U_{ij,k}(p, q) d_{ik}^{(n)}(q)] \, \mathrm{d}V_q^0 \\ & + \frac{\partial}{\partial x_I} \int_{B^0} U_{ij,m}(p, q) G_{mikn}(q) v_{k,n}(q) \, \mathrm{d}V_q^0 \\ & + \frac{\partial}{\partial x_I} \int_{B^0} U_{ij,m}(p, q) C_{mikn}(q) v_{k,n}(q) \, \mathrm{d}V_q^0. \end{aligned} \tag{44}$$

As before, one must be careful with differentiation of kernels like $U_{ij,m}$. The extra integrals in the large strain formulation, however, present no added difficulties relative to the small strain problem. Thus, all the earlier discussion regarding numerical evaluation of the domain integrals applies here, also. So far, numerical results from these equations have been obtained for planar and axisymmetric problems. In such cases, it has been possible to evaluate each of the volume integrals analytically (for a specific simple choice of shape

functions for the unknowns in these domain integrals) and then differentiate these integrals at an arbitrary source point p.

Once the velocity gradients and then d_{ij} have been determined, the nonelastic deformation rate $d_{ij}^{(n)}$ is subtracted from it to get the elastic deformation rate $d_{ij}^{(e)}$. The objective rate of the Cauchy stress in a coordinate system rotating with the material particle can then be obtained from eqn (7). Equation (8) will then be used to integrate this objective rate to obtain the Cauchy stress tensor at any instant of time.

2.5. *Plane-strain cases*

As before, the plane-strain equations can be obtained from the three-dimensional ones with $v_3 = 0$, $\partial/\partial x_3 = 0$, and using the corresponding fundamental solution with $u_3^{(B)} = 0$. This means that the left-hand side of eqn (16) is now summed only for $i, j = 1, 2$. The right-hand side of eqn (16) still retains the term $\sigma_{33}^{(B)} d_{33}^{(e)}$. Following the derivation of the three-dimensional equations, the plane-strain equation is

$$\begin{aligned} v_j(p) = &\int_{\partial B^0} [U_{ij}(p, Q)\dot{t}_i(Q) - T_{ij}(p, Q)v_i(Q)]\, \mathrm{d}S_Q^0 \\ &+ \int_{B^0} [\lambda U_{ij,i}(p, q)\eta^{(n)}(q) + 2GU_{ij,k}(p, q)d_k^{(n)}(q)]\, \mathrm{d}V_q^0 \\ &+ \int_{B^0} U_{ij,m}(p, q)G_{mikl}(q)v_{k,l}(q)\, \mathrm{d}V_q^0 \\ &+ \int_{B^0} U_{ij,m}(p, q)C_{mikl}(q)v_{k,l}(q)\, \mathrm{d}V_q^0, \end{aligned} \tag{45}$$

where, now, $\eta^{(n)} = d_{11}^{(n)} + d_{22}^{(n)} + d_{33}^{(n)}$ and the range of indices in eqn (45) is 1, 2. The plane-strain kernels U_{ij} and T_{ij} must be used. Using the convention

$$\{v_{k,l}\} = [v_{1,1} \quad v_{2,1} \quad v_{1,2} \quad v_{2,2}], \tag{46}$$

the matrix corresponding to G_{ijkl} for plane-strain is

$$[G] = \begin{bmatrix} \sigma_{11} & & & \\ \sigma_{12} & -\frac{1}{2}(\sigma_{11} - \sigma_{22}) & & \\ 0 & \frac{1}{2}(\sigma_{11} + \sigma_{12}) & -\frac{1}{2}(\sigma_{22} - \sigma_{11}) & \\ 0 & 0 & \sigma_{12} & \sigma_{22} \end{bmatrix}.$$

The components of C_{ijkl} can be easily obtained from eqn (25).

2.6. *Plane-stress cases*

The plane-stress situation considered here is that for a compressible metal. Although generally it is sufficient to consider $d_{kk}^{(n)} = 0$ for metal deformation (and hence $d_{kk} \cong = 0$), compressibility effects can be important in some situations, e.g. if the effect of distributed voids inside the metallic body is important.

For plane-stress, $\sigma_{13} = \sigma_{23} = \sigma_{33} = 0$. It is also usual to assume for plane-stress that $v_{1,3} = v_{2,3} = v_{3,1} = v_{3,2} = 0$ so that $\omega_{13} = \omega_{23} = 0$. This means that, from the definition of the objective rates [eqn (7)], $\overset{\square}{\sigma}_{13} = \overset{\square}{\sigma}_{23} = \overset{\square}{\sigma}_{33} = 0$. Thus, the left-hand side of eqn (16) need only be summed for $i, j = 1, 2$. The right-hand side, of course, must also be summed for $i, j = 1, 2$ and, here, $\varepsilon_{33}^{(R)}$ can be eliminated in favor of $\varepsilon_{11}^{(R)} + \varepsilon_{22}^{(R)}$, as for the small-deformation case. Finally, the resulting plane-stress equation can be expressed as

$$v_j(p) = \int_{\partial B^0} [U_{ij}(p, Q)\dot{t}_i(Q) - T_{ij}(p, Q)v_i(Q)]\,\mathrm{d}S_Q^0$$
$$+ \int_{B^0} [\bar{\lambda}U_{ij,i}(p, q)d_{kk}^{(\eta)}(q) + 2GU_{ij,k}(p, q)d_{ik}^{(\eta)}(q)]\,\mathrm{d}V_q^0$$
$$+ \int_{B^0} U_{ij,m}(p, q)G_{mikl}(q)v_{k,l}(q)\,\mathrm{d}V_q^0$$
$$- \int_{B^0} U_{ij,m}(p, q)\sigma_{mi}(q)\eta(q)\,\mathrm{d}V_q^0, \tag{47}$$

where the range of indices is $i, j = 1, 2$. The plane-stress kernels U_{ij} and T_{ij} must be used in the above. The plane-stress version of G_{mikl}, with the range of indices 1, 2, is the same as that for plane-strain. However,

$$\eta = d_{11} + d_{22} + d_{33}, \tag{48}$$

and it is convenient to eliminate d_{33} in terms of d_{11} and d_{22}. Using eqn (6) for $i = j = 3$ and $\overset{\square}{\sigma}_{33} = 0$, one gets

$$d_{33} = -\frac{\nu}{1-\nu}(d_{11} + d_{22}) + \frac{\nu}{1-\nu}[d_{11}^{(\eta)} + d_{22}^{(\eta)} + d_{33}^{(\eta)}]. \tag{49}$$

Thus, the presence of $d_{33}^{(\eta)}$ in eqn (47) cannot be avoided. For the incompressible plane-stress problem, however, the last integral in eqn (57) vanishes, and the equation is expressible only in terms of components in the 1- and 2-directions.

2.7. *Numerical implementation for planar cases*

Most of the earlier procedures regarding numerical implementation of the small-deformation BEM equations (Banerjee and Butterfield, 1981; Mukherjee, 1982) also apply here to the case of large deformation. A discretized version of eqn (43) for the velocity can now be obtained as

$$C_{ij}(P_M)v_i(P_M) = \sum_{N_S} \int_{\Delta S_N} [U_{ij}(P_{M,Q}\dot{t}_i(Q) - T_{ij}(P_M, Q)v_i(Q)]\,\mathrm{d}S_Q^0$$
$$+ \sum_{n_i} \int_{\Delta A_n} [\lambda U_{ij,i}(P_M, q)d_{kk}^{(\eta)}(q) + 2GU_{ij,k}(P_M, q)]d_{ik}^{(\eta)}(q)\,\mathrm{d}V_q^0$$
$$+ \sum_{n_i} \int_{\Delta A_n} U_{ij,m}(P_M, q)G_{mikl}(q)v_{k,l}(q)\,\mathrm{d}V_Q^0$$
$$+ \sum_{n_i} \int_{\Delta A_n} U_{ij,m}(P_M, q)\bar{C}_{mikl}(q)v_{k,l}(q)\,\mathrm{d}V_q^0, \tag{50}$$

where the boundary of the body in the reference configuration ∂B^0 is divided into N_S boundary segments and the interior into n_i internal cells, and $v_i(P_M)$ are the components of velocities at a point P which coincides with node M.

Suitable shape functions must now be chosen for the variation of tractions and velocities on the surface element ΔS_N and the variation of the nonelastic strain rates and velocities over an internal cell ΔA_n. Following essentially the same procedure as for small strain problems, one obtains the algebraic system

$$[A]\{v\} + [B]\{\dot{t}\} = \{b\}, \tag{51}$$

where the coefficient matrices $[A]$ and $[B]$ contain integrals of the kernels and the shape functions, and the vector $\{b\}$ contains the contributions of various quantities from the three domain integrals. Equations for the velocity field and the velocity gradients at an internal point are discretized in a similar fashion.

2.8. *Axisymmetric cases*

A BEM formulation for large strain–large rotation axisymmetric problems of elastoviscoplasticity is presented in this section (Rajiyah and Mukherjee, 1987; Chandra and Saigal, 1991; Chandra and Srivastava, 1991). The BEM formulation is capable of handling compressible plasticity effects ($d_{kk}^{(n)} \neq 0$). Let us consider an axisymmetric body under axisymmetric loading. Using cylindrical polar coordinates R, θ, and Z, the nonzero components of displacements, strains, and stresses are u_R, u_Z, ε_{RR}, $\varepsilon_{\theta\theta}$, ε_{ZZ}, ε_{ZR} $(= \varepsilon_{RZ})$, σ_{RR}, $\sigma_{\theta\theta}$, σ_{ZZ}, and σ_{RZ} $(= \sigma_{ZR})$. All the dependent variables are functions of R, Z, and time t. The notation used here is shown in Fig. 1. The source point is denoted by (R, O, Z) and the field point by (ρ, θ, ζ). Since the problem is axisymmetric, it is sufficient to consider a generating plane and to choose the source point in the x_1–x_3 plane. The three-dimensional kernels U_{ij}, T_{ij} etc. (Banerjee and Butterfield, 1981; Mukherjee, 1982), are integrated for the field point moving around a ring, keeping the source point fixed. Integrating θ from 0 to 2π results in ($j = 1$ and 3, no sum over ρ and ζ):

$$
\begin{aligned}
v_j = &\int_{\partial B^0} [U_{\rho j}\tau_\rho^{(L)} + U_{\zeta j}\tau_\zeta^{(L)} - T_{\rho j}v_\rho - T_{\zeta j}v_\zeta]\rho_0\,\mathrm{d}c_0 + \int_{B^0}\left\{\lambda\left[U_{\rho j,\rho} + U_{\zeta j,\zeta} + \frac{U_{\rho j}}{\rho_0}\right]d^{(n)}\right.\\
&\left. + 2G\left[U_{\rho j,\rho}d_{\rho\rho}^{(n)} + U_{\rho j,\zeta}d_{\rho\zeta}^{(n)} + U_{\zeta j,\rho}d_{\zeta\rho}^{(n)} + U_{\zeta j,\zeta}d_{\zeta\zeta}^{(n)} + \frac{U_{\rho j}d_{\theta\theta}^{(n)}}{\rho}\right]\right\}\rho_0 d\rho_0\,\mathrm{d}\zeta_0\\
&+ \int_{B^0}\left\{U_{\rho j,\rho}[\sigma_{\rho\rho}d_{\rho\rho} + \sigma_{\rho\zeta}(d_{\rho\zeta}\omega_{\rho\zeta}) - \sigma_{\rho\rho}d] + U_{\rho j,\zeta}[\sigma_{\rho\rho}d_{\rho\zeta} + \sigma_{\rho\zeta}d_{\zeta\zeta} - \sigma_{\zeta\zeta}\omega_{\rho\zeta} - \sigma_{\rho\zeta}d]\right.\\
&+ U_{\zeta j,\rho}[\sigma_{\rho\rho}\omega_{\rho\zeta} + \sigma_{\rho\zeta}d_{\rho\rho} + \sigma_{\zeta\zeta}d_{\rho\zeta} - \sigma_{\zeta\rho}d] + U_{\zeta j,\zeta}[\sigma_{\rho\zeta}(d_{\rho\zeta} + \omega_{\rho\zeta}) + \sigma_{\zeta\zeta}d_{\zeta\zeta} - \sigma_{\zeta\zeta}d]\\
&\left. + \frac{U_{\rho j}}{\rho_0}[\sigma_{\theta\theta}d_{\theta\theta} - \sigma_{\theta\theta}d]\right\}\rho_0 d\rho_0\,\mathrm{d}\zeta_0, \qquad (52a)
\end{aligned}
$$

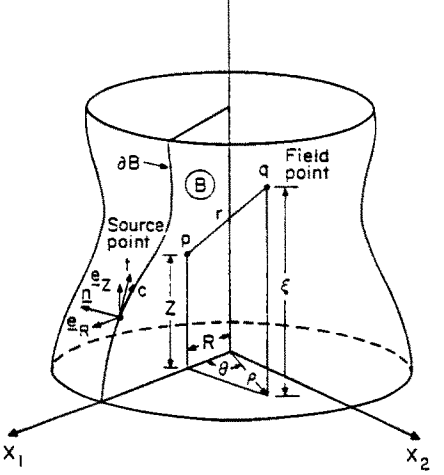

Source coords (R, O, Z)
Field coords (ρ, θ, ξ)
$r^2 = \rho^2 + R^2 + \xi^2 + Z^2 - 2R\rho\cos\theta - 2Z\xi$

Fig. 1. Geometry of the axisymmetric problem.

where

$$d^{(n)} = d_{\rho\rho}^{(n)} + d_{\theta\theta}^{(n)} + d_{\zeta\zeta}^{(n)} \tag{52b}$$

and

$$d = d_{\rho\rho} + d_{\theta\theta} + d_{\zeta\zeta}. \tag{52c}$$

Here, due to axisymmetry, $v_R = v_1$, $v_Z = v_3$, and $dc_0 = \sqrt{(d\rho^2 + d\zeta^2)}$ is an element on the boundary of the $\rho-\zeta$ plane. The domain B^0 and boundary ∂B^0 in the above equation now refer to a generator plane of the axisymmetric solid and its boundary (excluding the portion on the x_3-axis), respectively, so that the three-dimensional problem is effectively reduced to a two-dimensional one. Also, eqn (50) is valid for the velocity at an internal source point. The corresponding boundary integral equation can be obtained by taking the limit $p \to P$, where p is the source point of the domain B^0 and P lies on the boundary ∂B^0. This introduces the corner tensor C_{ij}. Deformation rate d_{ij} and spin ω_{ij} are defined as before [eqns (2)–(3)].

Material coordinates in the reference configuration and in the current configuration are denoted by X_i and x_i, respectively. It should also be noted here that the BEM formulation is written in an updated Lagrangian frame. The details of the kernels for $p \notin$ the axis of symmetry are given by Mukherjee (1982). Kernels for $p \in$ the axis of symmetry are given by Rajiyah and Mukherjee (1987). It is interesting to note, however, that kernels like $U_{\rho 1,\rho}$ for $p \in$ the axis of symmetry can be nonzero even though $U_{\rho 1}$ is equal to zero. These are determined by considering the appropriate components of the three-dimensional kernel $U_{ij,k}$, setting $R = 0$, and then integrating θ from 0 to 2π.

The Lagrangian traction rate $\tau_i^{(L)}$ [$\tau_i^{(L)} = n_j \dot{s}_{ji}$] deserves particular attention here. The traction rates can be written as:

$$\tau_\rho^{(L)} = \tau_\rho^{(c)} - n_\rho[\sigma_{\rho\rho} d_{\rho\rho} + \sigma_{\rho\zeta}(d_{\rho\zeta} - \omega_{\rho\zeta}) - \sigma_{\rho\rho} d] - n_\zeta[\sigma_{\rho\rho} d_{\rho\zeta} + \sigma_{\rho\zeta} d_{\zeta\zeta} - \sigma_{\zeta\zeta}\omega_{\rho\zeta} - \sigma_{\zeta\rho} d] \tag{53a}$$

and

$$\tau_\zeta^{(L)} = \tau_\zeta^{(c)} - n_\rho[\sigma_{\rho\rho}\omega_{\rho\zeta} + \sigma_{\rho\zeta} d_{\rho\rho} + \sigma_{\zeta\zeta} d_{\rho\zeta} - \sigma_{\rho\zeta} d] - n_\zeta[\sigma_{\rho\zeta}(d_{\rho\zeta} + \omega_{\rho\zeta}) + \sigma_{\zeta\zeta} d_{\zeta\zeta} - \sigma_{\zeta\zeta} d], \tag{53b}$$

where the Cauchy traction rate $\tau_i^{(c)}$ is given as

$$\tau_i^{(c)} = n_j \overset{\square}{\sigma}_{ji}, \tag{53c}$$

or

$$\tau_\rho^{(c)} = n_\rho \overset{\square}{\sigma}_{\rho\rho} + n_\zeta \overset{\square}{\sigma}_{\zeta\rho}, \tag{53d}$$

and

$$\tau_\zeta^{(c)} = n_\rho \overset{\square}{\sigma}_{\rho\zeta} + n_\zeta \overset{\square}{\sigma}_{\zeta\zeta}. \tag{53e}$$

A superposed square ($\overset{\square}{}$) implies the objective rate of a quantity, and $\tau_\rho^{(c)}$ and $\tau_\zeta^{(c)}$ may be interpreted as components of the rate of the prescribed follower force per unit deformed surface area on the deforming boundary. The follower force moves with a boundary point and rotates with the normal to the boundary at that point. Equations (53) can be interpreted as the "load correction" used by several researchers using FEM. A similar technique is used here to analyse axisymmetric extrusion problems by the BEM. The details of implementation of the load correction equations for axisymmetric extrusion are discussed in the following section on interface modeling.

Velocity gradients at an internal point are obtained here by differentiating eqn (52a) at an internal source point p. The term on the left-hand side of (52) becomes $v_{j,l}$. For the boundary integral on the right-hand side, the derivatives can be readily moved under the integral sign (since p is an internal point and Q is a boundary point, the differentiated boundary integral is regular). This, however, is not the case for the domain integrals in eqn

(52a) which are, in general, $1/r$ singular. The derivatives $\partial I/\partial x_l$, where I is either of the domain integrals on the right-hand side, can be evaluated using the method presented by Bui (1978). Free terms result in the process. A detailed discussion of the handling of free terms and a list are presented by Rajiyah and Mukherjee (1987). They also present an analytical/numerical technique for obtaining Cauchy principal values of integrals containing integrands with $1/r^2$ singularity. This approach is followed in the present work. Huang and Du (1988) have also proposed an alternative procedure for evaluating these strongly singular integrals.

Assuming that the elastic field obeys laws of hypoelasticity, and using eqns (6)–(7), it is a simple matter to obtain the objective and then the material rates of the Cauchy stress at an internal point once the velocity gradients have been determined at that point. In cylindrical polar coordinates, the relationship between the material and Jaumann rates of components of the Cauchy stress can be expressed as

$$\overset{\square}{\sigma}_{RR} = \dot{\sigma}_{RR} - 2\sigma_{RZ}\Omega_{RZ}, \tag{54a}$$

$$\overset{\square}{\sigma}_{\theta\theta} = \dot{\sigma}_{\theta\theta}, \tag{54b}$$

$$\overset{\square}{\sigma}_{RZ} = \dot{\sigma}_{RZ} + \sigma_{RR}\Omega_{RZ} - \sigma_{ZZ}\Omega_{RZ}, \tag{54c}$$

$$\overset{\square}{\sigma}_{ZZ} = \dot{\sigma}_{ZZ} + 2\sigma_{RZ}\Omega_{RZ}. \tag{54d}$$

It is important to note here that in an updated Lagrangian frame, $\boldsymbol{\Omega} = \boldsymbol{\omega}$. There are several algorithms for obtaining the boundary stress rates. The approach first suggested by Rizzo and Shippy (1968), and later extended to materially and geometrically nonlinear problems by Mukherjee (1982), required tangential differentiation of the velocity components at a boundary point. Recently, Okada *et al.* (1987) also proposed an alternative BEM formulation for large strain problems of elastoplasticity. This formulation is based on a weighted residual approach. If the velocity field for the fundamental solution is used as the weighting function, one obtains the formulation of Chandra and Mukherjee (1983, 1984a). The approach due to Rizzo and Shippy and Mukherjee and co-workers is used for obtaining the boundary stress rate presented here.

The normal and tangential components of the traction rate vector are first calculated at some point P on ∂B (P is assumed to lie at a point on ∂B where it is locally smooth). Now, in the local coordinate system $c-n$ (where c is tangential to ∂B at P),

$$\overset{\square}{\sigma}_{nn} = -\tau_n^{(c)} \tag{55a}$$

and

$$\overset{\square}{\sigma}_{nc} = -\tau_c^{(c)}, \tag{55b}$$

where $\overset{\square}{\sigma}_{nn}$ and $\overset{\square}{\sigma}_{nc}$ are the normal and shearing components of objective rates of Cauchy stress at P, respectively. The normal and tangential components of v_c and v_n are calculated next, and their tangential derivatives ($\partial v_c/\partial c$ and $\partial v_n/\partial c$) are obtained at P by numerical differentiation along the boundary element. The constitutive equations can then be written as

$$\frac{\partial v_c}{\partial c} = d_{cc} = \frac{1}{E}[\overset{\square}{\sigma}_{cc} - v(\overset{\square}{\sigma}_{nn} + \overset{\square}{\sigma}_{\theta\theta})] + d_{cc}^{(n)} \tag{56a}$$

and

$$\frac{v_R}{R} = d_{\theta\theta} = \frac{1}{E}[\overset{\square}{\sigma}_{\theta\theta} - v(\overset{\square}{\sigma}_{nn} + \overset{\square}{\sigma}_{cc})] + d_{\theta\theta}^{(n)}. \tag{56b}$$

The spin is given as

$$(\dot{t})_{cn} = (\dot{t})_{RZ} = \frac{\overset{\square}{\sigma}_{nc}}{2G} + d^{(n)}_{nc} - \frac{\partial v_n}{\partial c}. \tag{57}$$

The nonelastic deformation rates $d^{(n)}_{RR}$, $d^{(n)}_{\theta\theta}$, $d^{(n)}_{ZZ}$, and $d^{(n)}_{RZ}$ are known at P from the Cauchy stresses through an appropriate constitutive model. In the above, $(\dot{t})_{cn}$ is the spin at P, which is invariant with respect to coordinate transformation. Now, $d^{(n)}_{cc}$ and $d^{(n)}_{nc}$ are obtained as

$$d^{(n)}_{cc} = d^{(n)}_{RR}c_R^2 + d^{(n)}_{ZZ}c_Z^2 + 2d^{(n)}_{RZ}c_R + c_Z, \tag{58a}$$

and

$$d^{(n)}_{nc} = (d^{(n)}_{ZZ} - d^{(n)}_{RR})c_R c_Z + d^{(n)}_{RZ}(c_Z^2 - c_Z^2), \tag{58b}$$

where

$$c_R = c \cdot e_R \quad \text{and} \quad c_Z = c \cdot e_Z.$$

The quantities $\overset{\square}{\sigma}_{cc}$, $\overset{\square}{\sigma}_{\theta\theta}$, and ω_{RZ} are determined from eqns (56)–(57). The quantities $\overset{\square}{\sigma}_{RR}$, $\overset{\square}{\sigma}_{ZZ}$, and $\overset{\square}{\sigma}_{RZ}$ can then be evaluated from stress transformations:

$$\overset{\square}{\sigma}_{RR} = \overset{\square}{\sigma}_{nn}c_Z^2 + \overset{\square}{\sigma}_{cc}c_R^2 - 2\overset{\square}{\sigma}_{nc}c_R c_Z, \tag{59a}$$

$$\overset{\square}{\sigma}_{ZZ} = \overset{\square}{\sigma}_{cc} - \overset{\square}{\sigma}_{RR} + \overset{\square}{\sigma}_{nn}, \tag{59b}$$

$$\overset{\square}{\sigma}_{RZ} = (\overset{\square}{\sigma}_{cc} - \overset{\square}{\sigma}_{nn})c_R c_Z + \overset{\square}{\sigma}_{nc}(c_R^2 - c_Z^2). \tag{59c}$$

2.9. *Numerical implementation for axisymmetyric problems*

For numerical implementation, the first step, as usual, is to divide the boundary ∂B of an R–Z section of an axisymmetric body into N_s boundary segments and the interior into n_i internal cells. Denoting by $v_i(P_M)$ the components of the velocity at a point P which correspond to node M, a discretized version of the boundary equation [eqn (52) with $p \to P$; no sum over ρ, θ, ζ; and $j = 1$ and 3] can be written as

$$\begin{aligned} C_{ij}v_i(P_M) = {} & \sum_{N_s}\int_{\Delta c}[U_{\rho j}\tau^{(L)}_{\rho} + U_{\zeta j}\tau^{(L)}_{\zeta} - T_{\rho j}v_{\rho} - T_{\zeta j}v_{\zeta}]\rho_0\,\mathrm{d}c_0 \\ & + \sum_{n_i}\int_{\Delta A_n}\left\{\lambda\left[U_{\rho j,\rho} + U_{\zeta j,\zeta} + \frac{U_{\rho j}}{\rho_0}\right]d^{(n)} + 2G\left[U_{\rho j,\rho}d^{(n)}_{\rho\rho} + U_{\rho j,\zeta}d^{(n)}_{\rho\zeta} + U_{\zeta j,\rho}d^{(n)}_{\zeta\rho} + U_{\zeta j,\zeta}d^{(n)}_{\zeta\zeta}\right.\right. \\ & \left.\left. + \frac{U_{\rho j}d^{(n)}_{\theta\theta}}{\rho_0}\right]\right\}\rho_0 d\rho_0\,\mathrm{d}\zeta_0 + \sum_{n_i}\int_{\Delta\nabla_n}\left\{U_{\rho j,\rho}[\sigma_{\rho\rho}d_{\rho\rho} + \sigma_{\rho\zeta}(d_{\rho\zeta} - \omega_{\rho\zeta}) - \sigma_{\rho\rho}d]\right. \\ & + U_{\rho j,\zeta}[\sigma_{\rho\rho}d_{\rho\zeta} + \sigma_{\rho\zeta}d_{\zeta\zeta} - \sigma_{\zeta\zeta}\omega_{\rho\zeta} - \sigma_{\rho\zeta}d] + U_{\zeta j,\rho}[\sigma_{\rho\rho}\omega_{\rho\zeta} + \sigma_{\rho\zeta}d_{\rho\rho} + \sigma_{\zeta\zeta}\omega_{\rho\zeta} - \sigma_{\zeta\rho}d] \\ & \left. + U_{\zeta j,}[\sigma_{\rho\delta}(d_{\rho\zeta} + \omega_{\rho\zeta}) + \sigma_{\zeta\zeta}d_{\zeta\zeta} - \sigma_{\zeta\zeta}d] + \frac{U_{\rho j}}{\rho_0}[\sigma_{\theta\theta}d_{\theta\theta} - \sigma_{\theta\theta}d]\right\}\rho_0 d\rho_0\,\mathrm{d}\zeta_0. \end{aligned} \tag{60a}$$

A similar discretized equation can also be written for the velocity gradients $v_{j,I}(p)$ by differentiating eqn (52a) at an internal source p and discretizing. Differentiating eqn (52a), the left-hand side becomes $v_{j,I}(p)$. On the right-hand side, the boundary integral becomes

$$\int_{\partial B^0}[U_{\rho j,I}\tau^{(L)}_{\rho} + U_{\zeta j,I}\tau^{(L)}_{\zeta} - T_{\rho j,I}v_{\rho} - T_{\zeta j,I}v_{\zeta}]\rho_0\,\mathrm{d}c_0.$$

In the above expression, the derivatives have been moved under the integral sign. Since p is an internal point, Q is a boundary point, and the above integral is regular. This, however, is not the case for the domain integrals in eqn (52a), which are in general $1/r$ singular. The

derivatives $\partial I/\partial x_I$, where I is either of the domain integrals on the right-hand side of (52a), can be evaluated by the technique of Bui (1978). This approach gives rise to free terms. The appropriate free terms from the various derivatives of the displacement kernels for the cases $p \notin$ the axis of symmetry and $p \in$ the axis of symmetry are given in Tables 1 and 2, respectively. It is interesting to note the free terms for some first derivatives of $U_{\rho 1}$ and $U_{\rho 3}$ if $p \in$ the axis of symmetry.

Thus, for example, the explicit form of the equation for $v_{1,\Gamma}(p_k)$ can be written as (at the kth internal source point, no sum over ρ or ζ, $p_k \notin x_3$-axis),

$$v_{1,\Gamma}(p_k) = \sum_{N_s} \int_{\Delta c} [U_{\rho 1,\Gamma}\tau_\rho^{(L)} + U_{\zeta 1,\Gamma}\tau_\zeta^{(L)} - T_{\rho 1,\Gamma}v_\rho - T_{\zeta 1,\Gamma}v_\zeta]\rho_0 \, dc_0$$

$$+ \sum_{n_i} \int_{\Delta A_n - \Delta A_\eta} (p_k)\left\{ i\left[U_{\rho 1,\rho\Gamma} + U_{\zeta 1,\zeta\Gamma} + \frac{U_{\rho 1,\Gamma}}{\rho_0} \right] d^{(n)} \right.$$

Table 1. Free terms in the velocity gradient equations for the case $p \notin$ the axis of symmetry

Kernel	Free terms: Radial differentiation ($I = 1$)	Free terms: Axial differentiation ($I = 3$)
$U_{\rho 1,\rho}$	$\frac{5-8v}{16(1-v)G}$	0
$U_{\rho 1,\zeta}$	0	$\frac{7-8v}{16(1-v)G}$
$U_{\zeta 1,\rho}$	0	$-\frac{1}{16(1-v)G}$
$U_{\zeta 1,\zeta}$	$-\frac{1}{16(1-v)G}$	0
$U_{\rho 3,\rho}$	0	$-\frac{1}{16(1-v)G}$
$U_{\rho 3,\zeta}$	$-\frac{1}{16(1-v)G}$	0
$U_{\zeta 3,\rho}$	$\frac{7-8v}{16(1-v)G}$	0
$U_{\zeta 3,\zeta}$	0	$\frac{5-8v}{16(1-v)G}$

Table 2. Nonzero free terms in the velocity gradient equations for the case $p \in$ the axis of symmetry

Kernel	Free terms radial differentiation ($I = 1$)	Kernel	Free terms axial differentiation ($I = 3$)
$U_{\rho 1,\rho}$	$\frac{17-20v}{60(1-v)G}$	$U_{\rho 3,\rho}$	$\frac{1}{60(1-v)G}$
$U_{\rho 1,\zeta}$	$-\frac{1}{30(1-v)G}$	$U_{\zeta 3,\zeta}$	$\frac{7-10v}{30(1-v)G}$
$U_{\rho 1}$	$-\frac{1}{12(1-v)G}$	$U_{\rho 3}$	$-\frac{1}{12(1-v)G}$

$$+2G\left[U_{\rho 1,\rho\Gamma}d^{(n)}_{\rho\rho}+U_{\rho 1,\zeta\Gamma}d^{(n)}_{\rho\zeta}+U_{\zeta 1,\rho\Gamma}d^{(n)}_{\zeta\rho}+U_{\zeta 1,\zeta\Gamma}d^{(n)}_{\zeta\zeta}+\frac{U_{\rho 1,\Gamma}d^{(n)}_{\theta\theta}}{\rho_0}\right]\Bigg\}\rho_0 d\rho_0\,d\zeta$$

$$+i\left[\frac{5-8v}{16(1-v)G}-\frac{1}{16(1-v)G}\right]d^{(n)}(p_k)+\frac{5-8v}{8(1-v)}d^{(n)}_{\rho\rho}(p_k)-\frac{1}{8(1-v)}d^{(n)}_{\zeta\zeta}(p_k)$$

$$+\sum_{n_i}\int_{\Delta A_n-\Delta A_\eta(p_k)}\Big\{U_{\rho 1,\rho\Gamma}[\sigma_{\rho\rho}d_{\rho\rho}+\sigma_{\rho\zeta}(d_{\rho\zeta}-\omega_{\rho\zeta})-\sigma_{\rho\rho}d]$$

$$+U_{\rho 1,\zeta\Gamma}[\sigma_{\rho\rho}d_{\rho\zeta}+\sigma_{\rho\zeta}d_{\zeta\zeta}-\sigma_{\zeta\zeta}\omega_{\rho\zeta}-\sigma_{\rho\zeta}d]+U_{\zeta 1,\rho\Gamma}[\sigma_{\rho\rho}\omega_{\rho\zeta}+\sigma_{\rho\zeta}d_{\rho\rho}-\sigma_{\zeta\zeta}d_{\rho\zeta}-\sigma_{\zeta\rho}d]$$

$$+U_{\zeta 1,\zeta\Gamma}[\sigma_{\rho\zeta}(d_{\rho\zeta}+\omega_{\rho\zeta})+\sigma_{\zeta\zeta}d_{\zeta\zeta}-\sigma_{\zeta\zeta}d]+\frac{U_{\rho 1,\Gamma}}{\rho_0}[\sigma_{\theta\theta}d_{\theta\theta}-\sigma_{\theta\theta}d]\Big\}\rho_0 d\rho_0\,d\zeta_0$$

$$+\frac{5-8v}{16G(1-v)}\{\sigma_{\rho\rho}(p_k)d_{\rho\rho}(p_k)+\sigma_{\rho\zeta}(p_k)[d_{\rho\zeta}(p_k)-\omega_{\rho\zeta}(p_k)]-\zeta_{\rho\rho}(p_k)d(p_k)\}$$

$$-\frac{1}{16G(1-v)}\{\sigma_{\rho\zeta}(p_k)[d_{\rho\zeta}(p_k)+\omega_{\rho\zeta}(p_k)]+\sigma_{\zeta\zeta}(p_k)d_{\zeta\zeta}(p_k)-\sigma_{\zeta\zeta}(p_k)d(p_k)\}. \quad (60b)$$

Similarly, other components of the velocity gradient (for $p_k \notin x_3$-axis) and $p_k \in x_3$-axis can be evaluated. In eqn (60b), $\Delta A_\eta(p_k)$ is a circle of small radius η, centered at p_k, in the plane of the generator of the axisymmetric solid. The Cauchy principal values of these integrals, with $\eta \to 0$, must now be evaluated accurately. This, in general, is a formidable task since the integrands are $1/r^2$ singular. Rajiyah and Mukherjee (1987) have developed a novel analytical–numerical technique for accurately determining these integrals, and a similar approach is pursued here. Discussion of this integration scheme is avoided here for the sake of brevity. A detailed discussion of the analytical–numerical scheme for singular integration of $U_{ij,kl}$ over internal cells is given by Rajiyah and Mukherjee.

Suitable shape functions must now be chosen for the variation of velocity and traction rates along boundary elements and for the variation of $d^{(n)}_{ij}$ and $v_{i,j}$ over internal cells. It should be noted here that $\tau^{(L)}_i$ denotes Lagrangian traction rate. Thus, the present formulation involves velocity gradients in the domain integrals, as well as in the boundary integrals of eqn (60). As will be discussed later in the section on interface modeling, the Cauchy traction rate $\tau^{(c)}_i$ in the tangential direction at the tool–workpiece interface is obtained from a friction model. In the present work, the domain shape functions for $v_{i,j}$ are used to approximate those quantities at the boundary nodes, instead of using separate shape functions for $v_{i,j}$ on the boundary.

2.10. *Solution strategy*

The solution strategy for these planar and axisymmetric problems are similar and can be best explained by referring to Fig. 2. The discussion here is about compressible elastic–viscoplastic deformation of metals using a state variable-type constitutive model.

The presence of velocity gradients in the boundary traction rates and in some of the domain integrals requires iterations within each time step. As mentioned before, the unknown velocity gradient components occur in a domain integral for elastic–plastic problems, even for the case of small strain. Here, this situation occurs whether elastic–plastic or elastic–viscoplastic constitutive models are used. The solution strategy for these problems can be described as follows:

(a) The elasticity problem is first solved to obtain initial displacements. For this step, eqn (51) is solved with $\{b\} = 0$ for the unknown components of $\mathbf{u}$ and $\boldsymbol{\tau}$ in terms of the prescribed ones.

(b) The initial values of the displacement gradients are obtained from a truncated version of eqn (60a) with $d^{(n)}_k = 0$, $v_{k,n} = 0$, and $\mathbf{v}$ and $\dot{\boldsymbol{\tau}}$ replaced by $\mathbf{u}$ and $\boldsymbol{\tau}$ in the rest of the equation. The initial stresses are determined from strains through Hooke's Law. The

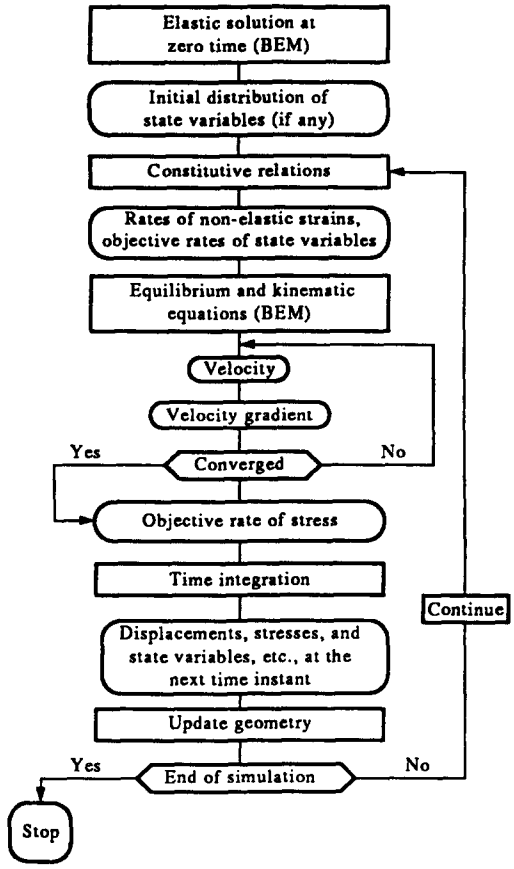

Fig. 2. Flow chart for the solution of large strain elastic–viscoplastic problems.

displacement gradients are used to form the deformation gradient matrix **F**. This matrix is decomposed according to the polar decomposition theorem $\mathbf{F} = \mathbf{RU}$, and **R** is obtained.

(c) The tensor $d_{ik}^{(n)}$ at zero time is obtained from the constitutive equations.

(d) The first approximation to $v_j(P)$ at $t = 0$ is calculated from the boundary equation for velocity with $v_{k,l}$ set to zero. It must be noted that the velocity gradients occur in two of the domain integrals, as well as in the expression for $\dot{\varepsilon}_i$.

(e) The first approximation to $v_{j,I}(p)$ at $t = 0$ is obtained from the velocity gradient equation with all the velocity gradients in the integrals on the right-hand side set to zero. The $v_{j,I}(p)$ values are extrapolated to get $v_{j,I}(P)$.

(f) The velocity gradients are inserted into the boundary equation and the full equation is solved to determine a second approximation to $v_j(P)$. This $v_j(P)$ and the first approximation of velocity gradients are then used to obtain a second approximation for $v_{j,I}(p)$.

(g) Step (f) is repeated until the required convergence is achieved and $v_j(P)$ is determined at zero time.

(h) The iterations are completed with $v_j(p)$, $v_{j,l}(p)$, $\overset{\square}{\sigma}_{ji}$, and $\overset{\square}{\varepsilon}_{ij}^{(a)}$ are calculated in the fixed global basis at zero time. The material derivative of **F** is determined from the equation $\dot{\mathbf{F}} = \mathbf{LF}$, where $L_{ij} = v_{i,j}$.

(i) Time integration is performed next. An explicit Euler-type scheme with proper time step controls (Kumar *et al.*, 1980) is used to find the relevant quantities, including **F**, at time Δt. **F** is decomposed into **RU** at time Δt, and **R** is obtained at Δt.

(j) The objective rates of the Cauchy stress and the anelastic strain are integrated in time. Here,

$$[\bar{\sigma}]_{t=\Delta t} = [\bar{\sigma}]_{t=0} + ([R]^T_{t=\Delta t}[\overset{\square}{\bar{\sigma}}]_{t=0}[R]_{t=\Delta t})\Delta t$$

$$[\sigma]_{t=\Delta t} = ([R][\bar{\sigma}][R]^T)_{t=\Delta t} \tag{61}$$

and similarly for $[\varepsilon^{(a)}]$.

Thus, the relevant quantities (displacements, displacement gradients, stresses, anelastic strains, etc.) are found at $t = \Delta t$. The time histories of various quantities are then obtained by marching forward in time and by suitable updating of the geometry and kernels. For cases involving relative small shear strains, time marching can also be carried out with the material derivatives of the tensor (obtained from objective, e.g. Jaumann, derivatives).

3. APPLICATIONS TO FORMING PROBLEMS

Applications of the above-cited BEM formulations to various planar and axisymmetric metal forming problems are presented in this section. Interface modeling of these processes is discussed and numerical results obtained by BEM are presented.

For both planar and axisymmetric problems, the BEM program uses straight boundary elements and polygonal internal cells. The velocity and traction rate are taken to be piecewise linear over the boundary elements, while the nonelastic deformation rate and the velocity gradients are assumed to be piecewise constant over the internal cells. The values of the boundary variables are assigned at nodes that lie at the intersections of boundary segments. Possible discontinuities in tractions are taken care of by placing a "zero length" element between nodes and assigning different values of traction at each of those nodes. All integrations of kernels are carried out analytically. The last two terms in eqn (44) are evaluated by first performing the integration over an internal cell for an arbitrary source point p_m and then differentiating the integral at p_m (Mukherjee, 1982; Chandra and Mukherjee, 1984a, 1987).

3.1. *Plane-strain extrusion*

Extrusion is a commonly used forming process. The shearing strains in an extrusion process are much smaller than unity. Accordingly, Jaumann rates utilizing the spin tensor can be used for objective rates of tensor quantities.

3.1.1. *Interface modeling.* Interface conditions at the die–workpiece boundary are considered here for problems of plane-strain extrusion. The assumptions are best explained in terms of a local coordinate system (α, β, γ). The origin of this coordinate system is positioned on the die–workpiece interface. The α-axis is tangential to the die surface and the β-axis is the outward normal to the die surface.

A consequence of the assumption of plane-strain is that

$$v_\gamma = 0, \quad \sigma_{\alpha\gamma} = \sigma_{\gamma\alpha} = \sigma_{\beta\gamma} = \alpha_{\gamma\beta} = 0. \tag{62}$$

It is further assumed that the contact or lubricant layer adjacent to the die surface cannot provide any resistance to tensile or compressive deformation. Thus, the scheme is equivalent to having an interface or bond element with zero stiffness in the direction tangential to the contact surface. Therefore,

$$\sigma_{\alpha\alpha} = 0, \tag{63}$$

so that only pressures and shear loadings get transferred across the interface and the stretch or compression of either the die or the workpiece is not transferred to the other. Another assumption made here is that the material is incompressible so that

$$d_{\alpha\alpha} + d_{\beta\beta} = 0 \quad (\text{since } d_{\gamma\gamma} = 0). \tag{64}$$

Using the above assumptions, zero normal velocity ($v_\beta = 0$), and the fact that the normal has components (0, 1, 0) in the local coordinate system, the load correction equation in the local coordinate system becomes

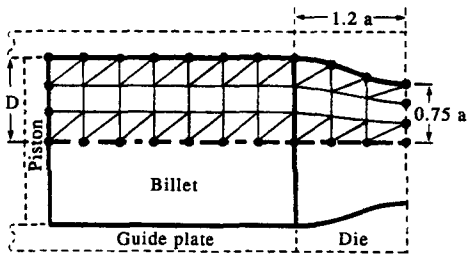

Fig. 3. Geometry of the plane-strain extrusion problem.

$$\dot{\tau}_\alpha = \mathring{\sigma}_{\alpha\beta} + \sigma_{\beta\beta}\omega_{\alpha\beta} + \sigma_{\alpha\beta}d_{\alpha\alpha}, \tag{65}$$

where a superposed asterisk indicates the Jaumann rate. The other traction component is assumed to vanish, i.e.

$$\dot{t}_\beta = 0. \tag{66}$$

The final assumptions relate to friction,

$$\mathring{\sigma}_{\alpha\beta} = \frac{G_s}{h}\mu v_\alpha \tag{67}$$

(where g_s and h are the shear modulus and the height of the interface element, respectively, and μ is the coefficient of friction), and

$$\omega_{\alpha\beta} = \kappa v_\alpha, \tag{68}$$

where κ is the local curvature.

The rate of the traction component, $\dot{\tau}_\alpha$, has now been obtained in terms of the tangential velocity v_α, its gradient in the tangential direction $v_{\alpha,\alpha}$, and the nonzero stress components $\sigma_{\alpha\beta}$ and $\sigma_{\beta\beta}$.

3.1.2. *Numerical results.* The primary purpose of obtaining the numerical results presented here is to demonstrate the ability of the boundary element method (BEM) to solve metal forming problems involving both geometric and material nonlinearities. Handling of the boundary conditions at the die interface requires special care for the extrusion problem. In the present BEM analysis, this can be incorporated quite easily through "load correction" [eqns (41)–(42)]. The material used is commercially pure aluminum at 24°C. The material parameters for Hart's model along with the experimental basis can be found in Alexopoulos (1981). The parameter $G_s/h = 1.268 \times 10^5$ MPa m^{-1}.

The geometry of planar extrusion considered here is shown in Fig. 3, and numerical results are presented in Figs 4–7. Figure 4 shows the steady-state distributions of the

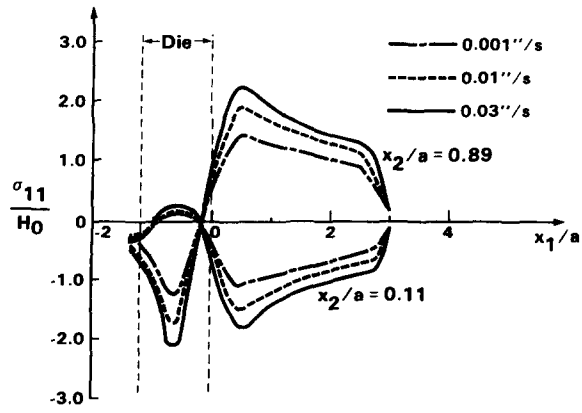

Fig. 4. Steady-state distribution of σ_{11} at different piston velocities for two values of X_2 ($\mu = 0$).

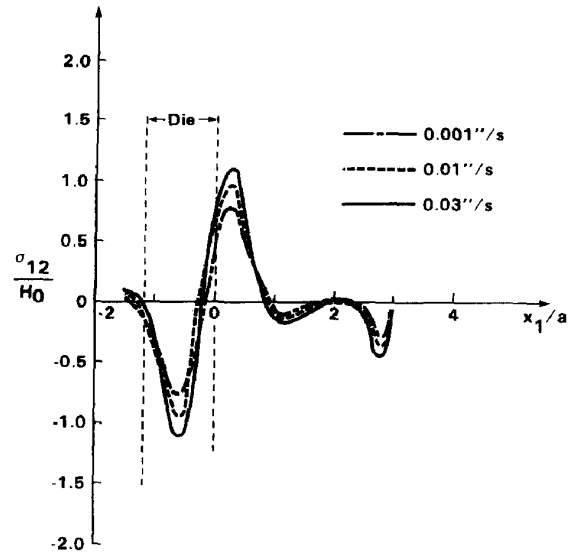

Fig. 5. Steady-state distribution of σ_{12} as functions of piston velocity ($\mu = 0.0$).

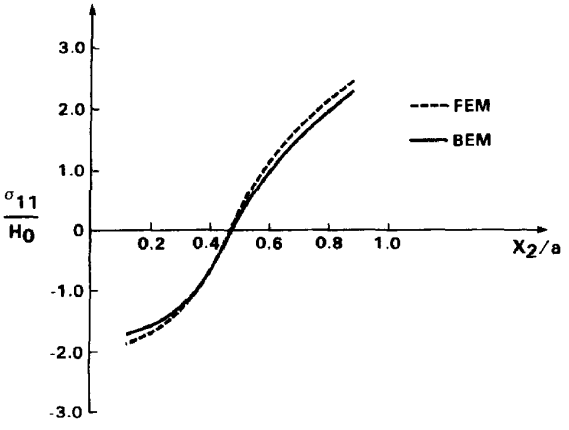

Fig. 6. Comparisons of residual stress distributions from BEM and FEM (piston velocity = 0.762 mm s^{-1}, $\mu = 0$).

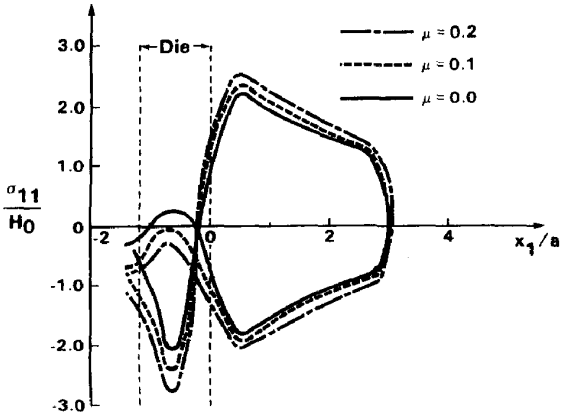

Fig. 7. Steady-state distributions of σ_{11} as functions of friction coefficient for two values of X_2 (piston velocity = 0.762 mm s^{-1}).

longitudinal stress σ_{11} for three different velocities in the absence of friction. In particular, the centerline of the workpiece is chosen to be the x_1-axis and the stress distributions are shown for material points in the deformed configuration, which initially had the same relative ordinate ($x_2/a = 0.11$ and 0.89) in the billet. Maximum residual tensile stress in an extruded workpiece is of crucial importance in design, since this is the primary potential source for crack initiation and growth. It is seen from Fig. 4 that the rate dependence of this quantity is quite significant. As the piston velocity is tripled from 0.254 mm s^{-1} to 0.762 mm s^{-1}, the BEM analysis predicts a change of 15.5% in the maximum longitudinal tensile stress in the workpiece. This compares well with the 17% change predicted by the FEM analysis (Chandra and Mukherjee, 1984b). The faster the billet is forced through the die, the less time there is for stresses to relax at material points in the workpiece as they move through the die. Consequently, the maximum longitudinal tensile stress upon exit from the die increases substantially with the speed of extrusion. Predictions of crucial effects like rate dependence of residual stresses is only possible through a detailed analysis using a realistic elastic–viscoplastic model for material behavior. It should be emphasized again that the material parameters for aluminum used in this calculation are those measured carefully by experiments (Alexopoulos, 1981).

Another important feature of elastic–viscoplastic analysis is that, following a peak value, the magnitude of σ_{11} decreases as a function of x_1 in most of the billet that has passed through the die. This is a result of stress relaxation in the workpiece after it is deformed, and the BEM predictions for such relaxations compare very well with those predicted by FEM analysis (Chandra and Mukherjee, 1984b).

The results for the steady-state distributions of shearing stress σ_{12} are shown in Fig. 5. It is seen that there is a marked variation of shearing stress inside and in the neighborhood of the die. Residual longitudinal stress distributions over a cross section ($x_1 = 0.4a$ from the die exit) from the two methods are shown in Fig. 6. It should be noted that these residual stress distributions must be self-equilibrating and, for the residual stresses obtained from the current BEM analysis, the error in satisfying equilibrium is about 5%.

The effect of friction on the results is depicted in Fig. 7. Three different values of friction are chosen for a piston velocity of 0.762 mm s^{-1}. The presence of friction increases the longitudinal stress peaks significantly. Of course, the friction model with constant coefficient of friction that is used here is crude at best, and much work remains to be done on modeling friction in metal forming processes. The present analysis does show, however, the effects of friction. The BEM predictions match quite well with FEM predictions of Chandra and Mukherjee (1984c).

3.2. *Profile rolling of gears*

The problem of profile rolling is considered next. This forming process involves rolling contact. Moreover, the shear strains can be high. Accordingly, care needs to be taken to avoid any spurious stress oscillations.

3.2.1. *Interface modeling.* Boundary conditions at the tool–workpiece interface are considered next. The working principle of the cold profile rolling process is shown in Fig. 8. Both rolling tools have the profile of the tooth space to be formed on the workpiece. These two profiled rolls rotate like planets about their orbital axes and can rotate either in the same direction (down-profile rolling) or in opposite directions (up-profile rolling) with respect to the feed of the workpiece. Due to this arrangement, the tools come in brief contact with the workpiece. The contact, occurring as a sudden stroke for a short period, is made once per tool revolution about the orbital axis. The work material is pushed radially from the tooth base toward the tooth top. During this forming operation, the workpiece does not rotate. As the tool moves away from it, the workpiece is turned by a tooth pitch and can also be advanced simultaneously in the longitudinal direction. Hence, the tool rolls and slides on the workpiece, and it is this combination of rolling and sliding that makes interface modeling quite difficult for profile rolling.

A considerable body of literature (Campos *et al.*, 1982; Martins and Oden, 1983; Pires and Oden, 1983; Torstenfelt, 1983; Bathe and Chaudhary, 1985) exists where sliding

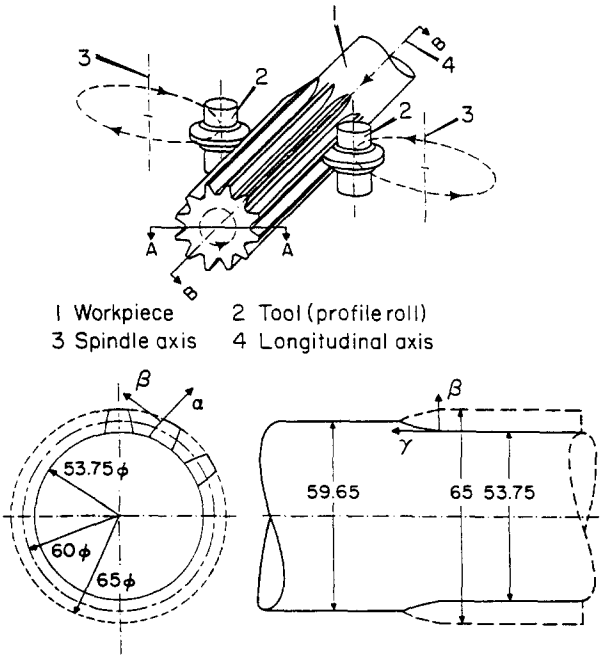

Fig. 8. Schematic diagram of the profile rolling process.

contact is handled in the FEM formulation by modifying the functional used in the variational principle. This typically introduces a Lagrange multiplier, or a penalty function, and gives rise to a mixed formulation. Zolti (1983) introduces an orthotropic gap element. It has been shown by Chandra and Mukherjee (1984b, c) that a gap or interface element can also be simulated within the original finite element through load correction. This smearing of the interface element keeps the geometric modeling simple (no need for extra interface elements) and retains the advantages of displacement formulations in FEM (positive definite stiffness matrix, ease of specifying boundary conditions, etc.).

Mukherjee and Chandra (1987) also applied the load correction technique to BEM. Since both displacements and tractions appear as unknowns, a BEM formulation is essentially a mixed one and is easily applicable in a contact situation. Here, the strategy of Mukherjee and Chandra is extended to include rolling contact situations as well.

The particular rolling contact model used here is the one proposed by Bhargava *et al.* (1985) and is based on the theory of Merwin and Johnson (1963). It was observed by Bhargava *et al.* that, for indentation loading (without rolling), the normal displacements under the center of contact are substantially larger than that predicted by the Hertzian theory. This larger displacement must be accompanied by an increase in the contact width in order to maintain continuity of the contacting surfaces. Also, the Merwin and Johnson analysis makes no attempt to satisfy the equilibrium requirements while rolling. The stress components acting at any depth below the surface are uncoupled from those acting at any other depth. Thus, any region that remains elastic in the Merwin and Johnson analysis is devoid of residual stresses, and equilibrium for a plane surface free from traction is attained at the end of every contact sequence by completely relaxing elastically the radial and shear residual stresses. Bhargava *et al.* make the analysis rigorous with respect to equilibrium and continuity requirements. The normal displacement differences of points at the center and edges of the two surfaces are required to be the same. This three-point continuity requirement increases the contact width. Accordingly, the Hertzian pressure distribution is modified. The total applied load, however, remains unaltered:

$$P = \int_{-a'}^{a'} p_0' \left[1 - \left(\frac{x^2}{a'^2} \right) \right]^{0.5} \mathrm{d}x = \frac{\pi p_0' a'}{2} = \frac{\pi p_0 a}{2}. \tag{69}$$

Here, P is the total applied load; p_0 and $2a$ are the Hertzian peak pressure and contact width, respectively; p_0' is the modified pressure peak; and $2a'$ is the modified contact width.

The interface conditions for profile rolling of gears can be best explained in terms of a local coordinate system (α, β, γ). The origin of this coordinate system is positioned at the tool–workpiece interface. The bottom left figure in Fig. 8 shows a section of the workpiece cut perpendicular to the direction of the feed. The α-axis is tangential to the interface at this section, and the β-axis is outward normal to the workpiece surface at this section. The γ-axis is perpendicular to this section and is along the direction of the axial feed of the workpiece. The bottom right figure in Fig. 8 shows another section of the workpiece parallel to the direction of the feed. It may be observed that the γ-axis is also tangential to the planetary motion of the tool and represents the direction of rolling.

Accordingly, the rolling contact occurs in the $\beta\gamma$ plane. Here, plane-strain conditions are assumed for rolling contact. The rolling contact is also assumed to be frictionless. Bhargava *et al.* (1985) translate the modified pressure distribution along the rolling direction. In profile rolling, however, the displacement boundary conditions are specified. As shown in the bottom right figure in Fig. 8, the depth of bite can also vary within a single forming stroke. Hence, the rolling contact situation is modeled by translating the appropriate displacement distribution in the $\beta\gamma$ plane along the γ-direction. Unlike the model of Bhargava *et al.*, the pressure distribution and total load are not known *a priori* in this case but are calculated for each increment of translation. Once the complete pressure distribution is obtained from the displacement distribution, the rolling contact model of Bhargava *et al.* is used to obtain the corresponding displacements, and the procedure is repeated until convergence. Upon convergence, the pressure distribution is integrated in space over the entire bite and a resultant load is obtained. The rate of this loading is stored and is later used as $i\beta$ for analysis of deformation in the $\alpha\beta$ plane.

Most of the sliding at the tool–workpiece interface, as well as the deformation of the workpiece, is expected to occur in the $\alpha\beta$ plane. It is also the deformation pattern in the $\alpha\beta$ plane that determines the shape of the gear teeth. For the analysis in the $\alpha\beta$ plane, it is assumed that $v_\gamma = 0$. Thus, a plane-strain situation arises.

Hence, the model of profile rolling presented here is a combination of the two plane-strain models. The rolling contact between the tool and the workpiece occurs in the $\beta\gamma$ plane, whereas the sliding of the material that directly influences the deformation pattern and the shape of the gear teeth takes place in the $\alpha\beta$ plane. Thus, the following BEM analysis and the results pertain to the $\alpha\beta$ plane and assume plane strain conditions in that plane. However, the rolling contact model (in the $\beta\gamma$ plane) determines the applied traction at the interface and thus influences the BEM analysis in the $\alpha\beta$ plane.

A consequence of the plane-strain assumption in the $\alpha\beta$ plane is that $v_\gamma = 0$ and $\sigma_{\alpha\gamma} = \sigma_{\gamma\alpha} = \sigma_{\beta\gamma} = \sigma_{\gamma\beta} = 0$. It is further assumed that the simulated interface element has zero stiffness in the direction tangential to the contact surface; therefore, only pressures and shear loadings get transferred across the interface. Hence, $\sigma_{\alpha\alpha} = 0$ at the interface.

Using the above assumptions, zero normal velocity at the interface ($v_\beta = 0$), and the fact that the normal has components (0, 1, 0) in the local coordinate system, the load correction equation in the local coordinate system at the interface can be written as

$$\dot{\tau}_\alpha = \dot{t}_\alpha + \sigma_{\beta\beta}\omega_{\alpha\beta} - \sigma_{\alpha\beta}d_{\beta\beta} - \sigma_{\alpha\beta}(d_{\alpha\alpha} + d_{\beta\beta}) \tag{70}$$

and

$$\dot{\tau}_\beta = \dot{t}_\beta - \sigma_{\alpha\beta}\omega_{\alpha\beta} - \sigma_{\alpha\beta}d_{\alpha\beta} - \sigma_{\beta\beta}d_{\beta\beta} - \sigma_{\beta\beta}(d_{\alpha\alpha} + d_{\beta\beta}). \tag{71}$$

The local rotation rate on the interface is defined as

$$\omega_{\alpha\beta} = \kappa v_\alpha, \tag{72}$$

where κ is the local curvature. It should be noted, however, that eqns (70)–(72) are valid only in an updated Lagrangian frame.

Here, $\dot{t}_\beta$ is obtained from the rolling contact model in the β_γ plane. As mentioned earlier, the rolling contact in the $\beta\gamma$ plane is assumed to be frictionless. Once the time history of the pressure distribution is obtained from the rolling contact model, the time derivative

of the pressure distribution and the resulting rate of loading are obtained. Next, the work-equivalent traction rates are obtained at nodal points in the $\alpha\beta$ plane and are transformed to the appropriate coordinate system to get $\dot{t}_\beta$.

Much research effort is currently focused upon the development of appropriate sliding mechanisms. Considering the development of our algorithm we should use a friction model that is physically realistic and easily extendable as more information becomes available. Coulomb's law of friction with μ_s as the static coefficient of friction and μ_d as the dynamic (or kinetic) coefficient of friction fulfills these criteria.

For the particular problem considered here, it is assumed that sliding occurs in the $\alpha\beta$ plane only. If t_α represents the developed tangential tractions along the interface, we assume that there is no relative motion between two adjacent particles on the tool and the workpiece as long as $|t_\alpha| \leqslant \mu_s t_\beta$ (t_β = compressive normal traction). The maximum traction of static friction is the smallest force necessary to start motion. During motion, the magnitude of the tangential traction resisted by friction is $\mu_d t_\beta$ (with $\mu_d \leqslant \mu_s$). The motion continues as long as the frictional traction developed is equal to $\mu_d t_\beta$. Once the developed tangential traction drops below the dynamic friction $\mu_d t_\beta$, the relative motion between the tool–workpiece interfaces ceases until such time that, again, the developed tangential traction exceeds the frictional capacity.

Since the material is incompressible and the normal at the tool–workpiece interface has components (0, 1, 0), the developed tangential traction rate can be obtained as

$$\dot{t}_\alpha = \overset{\square}{\sigma}_{\alpha\beta}. \tag{73}$$

The developed tangential traction (t_α) is compared to the frictional capacity to determine sticking or sliding situations.

3.2.2. *Numerical results.* The rolling contact problem is solved first and iterated until convergence is obtained. The normal traction rate $\dot{t}_\beta$ is obtained for later use in the plane-strain BEM analysis. In the BEM analysis, the velocity gradient in the previous time step is used as a first guess at each time step and iterated until convergence.

The geometry of the plane-strain forming problem is shown in Fig. 9. Initial blank diameter is 59.65 mm. The pitch diameter is 60 mm. Addendum and dedendum diameters are 65.0 mm and 53.75 mm, respectively. The teeth have a pressure angle of 20°. The material used is AISI 1045 heat-treatable steel. As shown by Eggert and Dawson (1987) and Mukherjee (1982), the material data (Bardes, 1978; Lange and Kurz, 1984) are fitted to Hart's state variable model. The state variable model parameters for AISI 1045 steel are found to be:

$$E = 1.07 \times 10^6 \text{ MPa } (3 \times 10^7 \text{ psi}), \quad \nu = 0.3$$
$$\lambda = 0.15, \quad M = 7.8, \quad m = 5.0$$
$$M = 1.2 \times 10^6 \text{ MPa } (1.74 \times 10^8 \text{ psi})$$

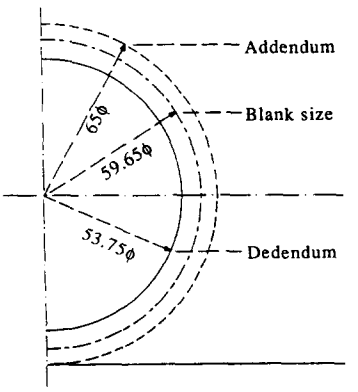

Fig. 9. Workpiece geometry for profile rolling.

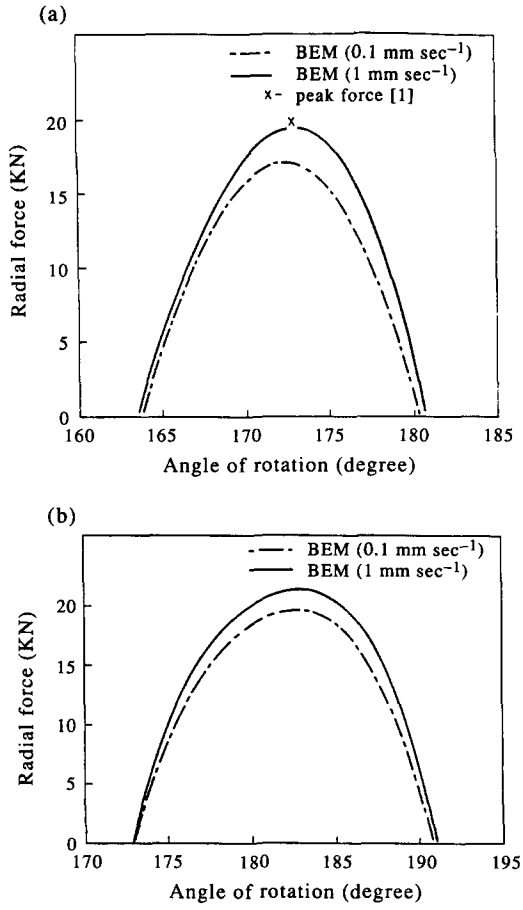

Fig. 10. Radial forming forces in profile rolling ($\mu_s = \mu_d = 0$): (a) down-profile rolling; (b) up-profile rolling.

(*)

$$d_{ST} = 1.4 \times 10^{-41}\,\mathrm{s}^{-1} \quad \text{at} \quad \sigma_S = 68.95\ \mathrm{MPa}\ (10^4\ \mathrm{psi})$$

$$d_0 = 3.15\,\mathrm{s}^{-1} \quad \text{at} \quad \sigma_0 = 68.95\ \mathrm{MPa}\ (10^4\ \mathrm{psi})$$

$$\beta = 0.910 \times 10^3\ \mathrm{MPa}\ (0.132 \times 10^6\ \mathrm{psi}), \quad \delta = 1.20.$$

The initial values of the state variables are:

$$H(\mathbf{x}, 0) = 600\ \mathrm{MPa}\ (87 \times 10^3\ \mathrm{psi})$$

$$\varepsilon_{ij}^{(a)}(\mathbf{x}, 0) = 0.0.$$

As the tool comes in contact with the workpiece at the tooth spaces, the material is pushed in toward the dedendum. As a result, material movement is induced and the material between two spaces is pushed out to the addendum—thus forming the gear teeth.

Figure 9 shows a symmetric half of the workpiece geometry. As the tool forms a particular tooth space, the two adjoint flanks are partially formed. A tooth flank becomes fully developed when both of its adjoint tooth spaces are formed completely. As shown in Fig. 8, two formed tools situated diametrically opposite each other are used. Three consecutive tooth spaces are formed in the symmetric half of the blank to study mutual influences of neighboring tooth spaces. This also develops the fully formed tooth flanks. Thus, the analysis for the formation of three consecutive tooth spaces is considered sufficient to understand the basic mechanics of profile rolling of gears.

Figure 10 shows the radial forces as a function of tool position for two different tool penetration velocities. As the tool penetrates into the workpiece, the radial forces rise

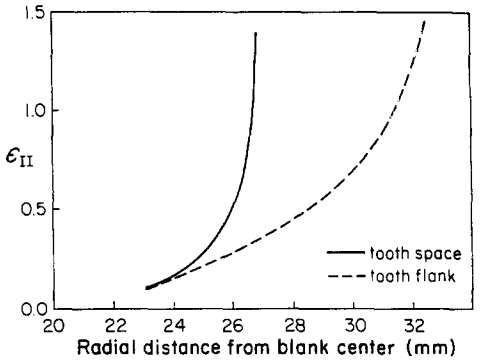

Fig. 11. Radial variation of equivalent strain in profile rolling ($\mu_s = \mu_d = 0$).

rapidly. For down-profile rolling, the peak occurs about 5–10° before the tool reaches its lowest position [as shown in Fig. 10(a)]. As observed in Fig. 10(b) for up-profile rolling, the peak radial force occurs just after the tool attains its lowest position. It can be distinctly recognized that in down-profile rolling, the forming process is completed shortly after the tool passes through its lowest point. On the other hand, for up-profile rolling, the maximum force occurs at this point. The resistance to rolling is greater in up-profile rolling. This is manifested in the higher maximum radial force for up-profile rolling. In down-profile rolling, the contact zone between the tool and the workpiece is larger compared to the corresponding contact zone in up-profile rolling. After passing through the maxima, the radial forces decrease rapidly for both down- and up-profile rolling. This drastic fall can be ascribed to the rapid reduction in tool bite. The peak force obtained from the BEM analysis for down-profile rolling compares well with the peak force obtained by Lange and Kurz (1984). The BEM analysis predicts the peak force to be 20 kN, while Lange and Kurz observed the peak force to be 21.78 kN. This difference is quite small, considering the fact that the material parameters used here only approximate the behavior of the material used by Lange and Kurz. For both down- and up-profile rolling, increasing the total penetration velocity by an order of magnitude increases the peak radial force by about 12%.

As the tool penetrates the workpiece, it induces extreme deformations near the periphery. Figure 11 shows the variations of equivalent strain ε_{II} (second invariant of Almansi strain) over radial lines over a tooth space, as well as a tooth flank. In both cases, the strain is heavily concentrated near the periphery. Along a radial line over a tooth space, ε_{II} drops from a peak value of 1.42 to 0.1 as we move just 4 mm inside. Along a radial line over a tooth flank, ε_{II} also drops from 1.44 to less than 0.1 over a radial distance of 9.5 mm. The magnitude and distribution of ε_{II} are found to change very little as the tool velocity is varied.

Figure 12 shows the variations of σ_{II} (second invariant of Cauchy stress) along radial

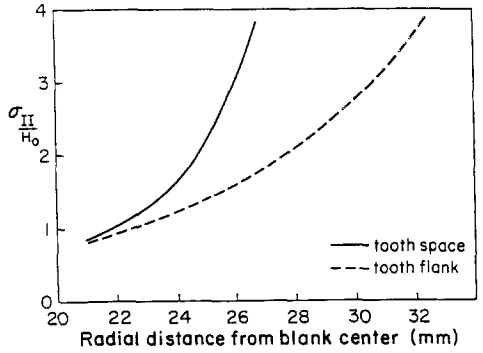

Fig. 12. Radial variation of equivalent stress in profile rolling ($\mu_s = \mu_d = 0$).

lines over a tooth space and a tooth flank. In both situations, σ_{II} rises sharply as we approach the periphery. As the radial distance decreases from 26.875 mm (periphery of tooth space) to 21 mm, σ_{II}/H drops from a peak value of 3.8 to about 0.9. Along a radial line over the tooth flank, σ_{II}/H drops from 3.9 at the tip of the tooth to 1.75 at the root of the tooth. It is evident that severe deformation near the periphery results in very high strain-hardening of the material at the periphery. This is desirable since the strain-hardening hardens the gear teeth. This also improves the endurance limit of the formed gear teeth.

The effect of friction on the circumferential distribution of ε_{II} is shown in Fig. 13. The origin represents the center of a tooth flank, and a circumferential distance of 1.25 π represents the center of the next tooth space. For complete sticking at the tool–workpiece interface ($\mu = \infty$), there is no flow of the material in the circumferential direction. At tooth spaces, the material is pushed inward and, as a consequence, the material in between is pushed up. However, at high friction, the material cannot flow easily in the circumferential direction. Hence, extreme shear deformation occurs at the boundary between a tooth space and tooth flank and can induce cracking. Proper lubrication of the interface alleviates this problem. Lubricating the interface reduces the coefficient of friction and smoothes the circumferential distribution of ε_{II}. As seen in Fig. 13, ε_{II} is higher at the boundary between a tooth space and tooth flank than at the centers of the space and flank regions. At $\mu = 0.0$, the distribution is almost uniform, with ε_{II} equal to 1.76 at the boundary between the two regions. At $\mu = 0.2$, however, the distribution gets sharper, with ε_{II} equal to 2.58 at the region boundary. At $\mu = 0.3$, the peak value of ε_{II} rises to about 3.125. Thus, at higher frictions, the shearing action gets localized rapidly.

3.3. *Plane-strain slab rolling*

A unique feature of slab rolling processes (shown schematically in Fig. 14) is the existence of a neutral point (or region) along the tool–workpiece interface where the tangential relative velocity between the deforming material and the tool becomes zero. The frictional stresses usually change direction at this neutral point (or region). The location of this neutral point or zone, however, is not known *a priori*. Accordingly, care must be taken to model this phenomenon appropriately.

3.3.1. *Interface modeling.* In addition to plane-strain assumptions [eqns (62)–(64)], the sliding contact at the roll–workpiece interface can be represented as

$$\sigma_{\alpha\beta} = -\mu_s \sigma_{\beta\beta} \left\{ \frac{2}{\pi} \tan^{-1} \left(\frac{|V_r|}{a} \right) \right\} \frac{V_r}{|V_r|} \tag{74}$$

(Chen and Kobayashi, 1978; Li and Kobayashi, 1982), where V_r is the relative velocity

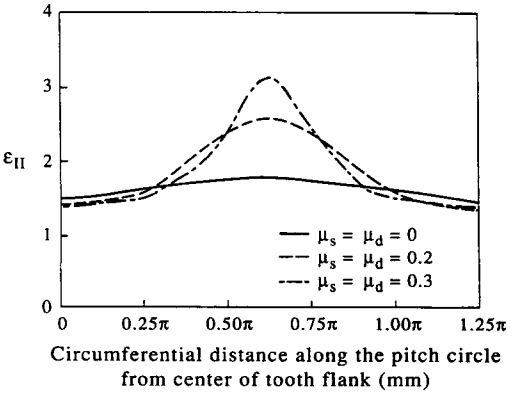

Fig. 13. Circumferential variation of equivalent strain in profile rolling at different friction coefficients.

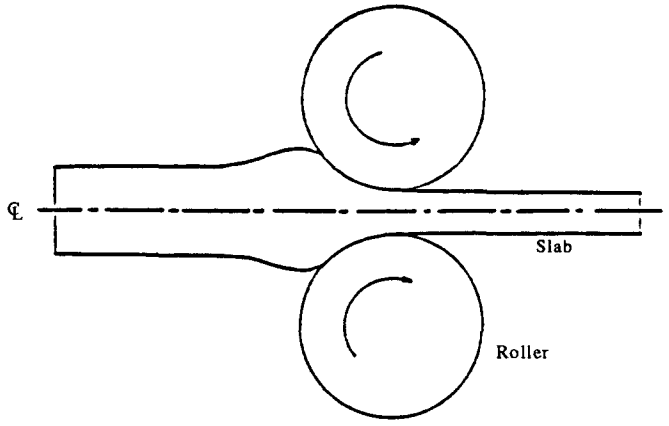

Fig. 14. Schematic diagram of plane-strain rolling.

between the roll and the workpiece in the tangential direction (α-direction), "a" is a constant several orders of magnitude smaller than the roll velocity, and μ_s is the static coefficient of friction. At the beginning of the roll bite, the velocity of the workpiece is zero. Hence, V_r is large (equal to the tangential velocity of the roll surface). Thus, $\sigma_{\alpha\beta} = -\mu_s\sigma_{\beta\beta}$, which represents the case of static friction. As the process of rolling continues, the workpiece is driven by the rolls and the relative velocity between the roll and the workpiece tends to decrease. Finally, a point (or region) is reached where the workpiece has reached the velocity of the roll. This point (or region), where the relative velocity at the roll–workpiece interface is zero, is called the neutral point (or region). At the neutral point, there is no shear transfer between the roll and the workpiece. Thus, $\sigma_{\alpha\beta}$ at this point drops to zero. Beyond this point, the workpiece tends to move faster than the roll, and the sense of $\sigma_{\alpha\beta}$ at the interface reverses. Accordingly, the developed tangential traction also reverses direction at this point.

While the friction models of Chen and Kobayashi (1978) and Li and Kobayashi (1982) represent the phenomenon of a neutral point quite well, they relate tangential traction rather than the tangential traction rate to the relative velocity. This is consistent with Coulomb's law of friction. The BEM formulation, however, is in rate form. In the case of plane-strain rolling, we can also show that

$$\dot{t}_\alpha = \overset{\square}{\sigma}_{\alpha\beta} \tag{75}$$

since the material is incompressible and the normal at the tool–workpiece interface has components (0, 1, 0). Thus, knowing $\sigma_{\alpha\beta}$ and the size of the time step, we can estimate $\dot{t}_\alpha$. This estimated value of $\dot{t}_\alpha$ is incorporated into the load correction equations and the assembled BEM equation is solved for the unknown velocities and traction rates (Chandra and Mukherjee, 1987). The estimate of $\dot{t}_\alpha$ is updated, and the scheme marches forward in time.

3.3.2. *Numerical simulation.* All integrations of kernels are carried out analytically. The two additional kernels (for nonlinearities) are evaluated by first performing the integration over an internal cell for an arbitrary source point p_m and then differentiating the integral at p_m. Time integration for the rolling problem is carried out by an explicit Euler-type method and an implicit ABM method with proper controls (Chandra, 1986).

The solution strategy, in essence, consists of marching forward in real time with suitable updating of the configuration of the body. The presence of velocity gradients in the boundary traction rates and in the domain integral for geometric nonlinearity requires iterations within each time step. Body force rate is assumed to be zero. However, this assumption can be waived without any difficulty. In the BEM analysis, the velocity gradient in the previous time step is used as a first guess at each time step and is iterated until convergence (Chandra and Mukherjee, 1984a, 1985, 1987; Mukherjee and Chandra, 1987). At the very first time step, the velocity of the workpiece is assumed to be zero, and the friction model (Chen and

Kobayashi, 1978; Li and Kobayashi, 1982) is used to obtain the value of the developed tangential traction (t_α). Later on, at any time step, the velocities of the contacting nodes of the workpiece in the previous time step are used to estimate V_r and a new estimate of t_α is obtained. Knowing the value of t_α at the beginning of the time step, the size of the time step, and the desired value of t_α at the end of the time step, $\dot{t}_\alpha$ during the time step is estimated and used in the BEM analysis.

The geometry of the plane-strain rolling problem considered here is shown in Fig. 14. The initial thickness of the workpiece is 10 mm. The horizontal contact length of the roll bite is 40 mm. Final thickness of the workpiece is 7.5 mm. The material used is commercially pure aluminum at a temperature of 24°C. The details of the parameters for Hart's model for this material and their significance are given by Alexopoulos (1981), Chandra and Mukherjee (1984b) and Chandra (1986).

The process of rolling is nonsteady-state at the beginning of a bite. It becomes steady-state as a material is rolled through the gap between the two rolls. The rollers have a constant angular velocity and compress the material as it is driven through the roll bite. As the workpiece comes in contact with the rollers, an interfacial friction force develops and the workpiece is drawn into the roll bite. Free-surface conditions are assumed on each side of the bite.

Figure 15 shows the variations in Almansi strains along the centerline of the workpiece as it passes through the roll bite. The thickness reduction here is 25%. It is interesting to note the small amount of material buildup just before the entrance into the roll bite. Due to this phenomenon, ε_{xx} is initially negative before entrance into the roll bite. As the material is gradually drawn between the rollers and the slab thickness is reduced, ε_{xx} becomes tensile. It reaches a peak value of 0.29 and drops slightly as the material passes by the rollers and the thickness increases due to springback. The strain variations shown in Fig. 15 qualitatively agree quite well with the strain fields obtained by Dawson (1987) from a viscous flow-type analysis. To avoid numerical instabilities, Dawson constrained the material velocity beyond the exit from the roll bite to be horizontal. In the present analysis, however, traction-free conditions are assumed. This allows proper springback of the material.

The normal pressure distributions between the roll and the workpiece at different roll velocities are shown in Fig. 16. For 25% reduction, the distribution is of the friction hill type. As the roll velocity increases from 1 to 10 mm s^{-1}, the peak normal pressure changes from 128–137 MPa. Also, the position of the peak shifts slightly toward the exit of the roll bite from $x/L = 2.5$ to $x/L = 2.67$. The normal pressure distributions compare quite well qualitatively to those obtained by Li and Kobayashi (1982) and Mori *et al.* (1982) from a rigid-plastic finite element analysis.

Figure 17 shows the shear stress distributions at the roll–workpiece interface at two different roll velocities. As the workpiece enters the roll bite, the relative velocity between

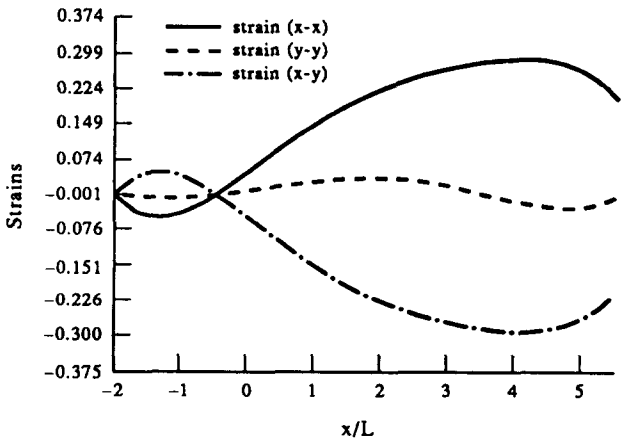

Fig. 15. Variations of strains along the centerline [—— strain (x–x); – – – strain (y–y); –·– strain (x–y)].

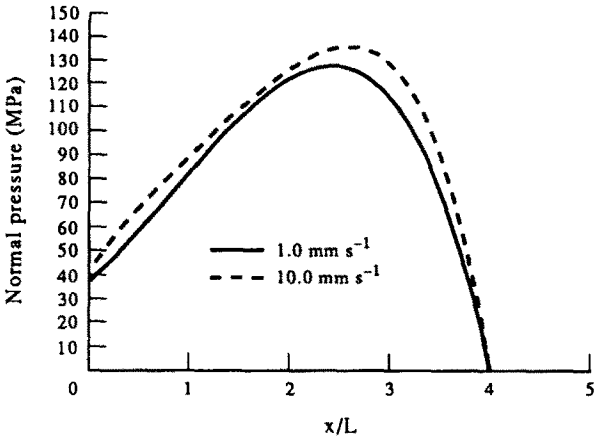

Fig. 16. Distributions of normal pressures at different roll velocities ($\mu = 0.10$; —— 1.0 mm s^{-1}; – – – 10.0 mm s^{-1}).

the workpiece and the roll is large. Accordingly, the shear stress is large. Once the workpiece has entered the bite, the normal pressure increases and the relative velocity decreases. Initially, the increase in normal pressure dominates and the shear stress goes up to a peak value of 6.7 MPa for a roll velocity of 1.0 mm s^{-1} (for $\mu = 0.1$). Then, the decrease in relative velocity causes the shear stress to drop and at $x/L = 2.58$, the shear stress changes direction. At this point, the relative velocity between the roll and the workpiece is negligible and this point (or region) is called the neutral point (or region). The shear stress reaches a value of -6.66 MPa before rising to zero at the exit from the roll bite. At a higher roll velocity of 10 mm s^{-1}, the neutral point shifts toward the exit and occurs at $x/L = 2.71$. The stress peaks also increase to $+9.6$ and -7.67 MPa. An increase in interface friction also moves the neutral point toward the exit. As the friction coefficient goes from 0.10 to 0.15, as shown in Fig. 18, the position of the neutral point moves from $x/L = 2.7$ to $x/L = 3.0$. For a roll velocity of 10 mm s^{-1}, the first peak rises from $+9.6$ to $+13.33$ MPa. However, the other peak changes from -7.67 MPa to only -8.33 MPa. The qualitative nature (or shape) of the shear stress distribution along the roll bite is not affected much by variations in roll velocity or interface friction.

Figure 19 shows the residual longitudinal stress distribution across the cross section of the workpiece at the exit from the roll bite. The residual σ_{xx} is tensile at the top and bottom faces and compressive at the center. As the roll velocity increases from 1.0 to

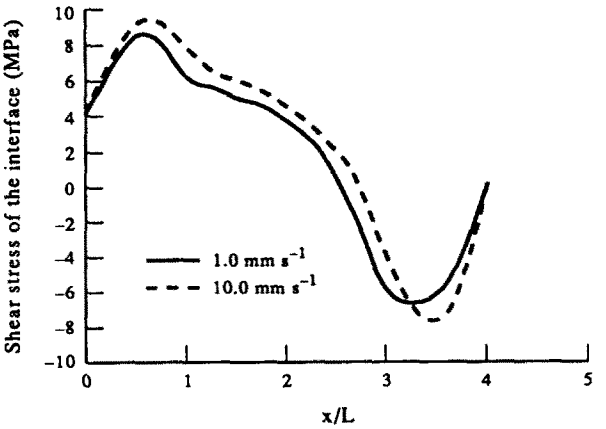

Fig. 17. Distributions of shear stress at the roll–workpiece interface ($\mu = 0.10$; —— 1.0 mm s^{-1}; – – – 10.0 mm s^{-1}).

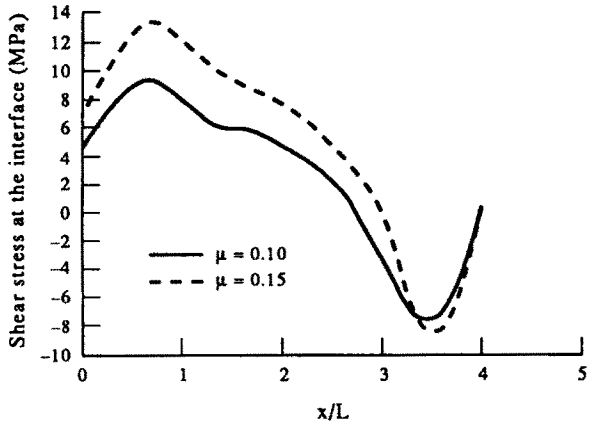

Fig. 18. Variations of shear stress at the interface with the frictional condition (roll velocity = 10 mm s^{-1}; —— $\mu = 0.10$; – – – $\mu = 0.15$).

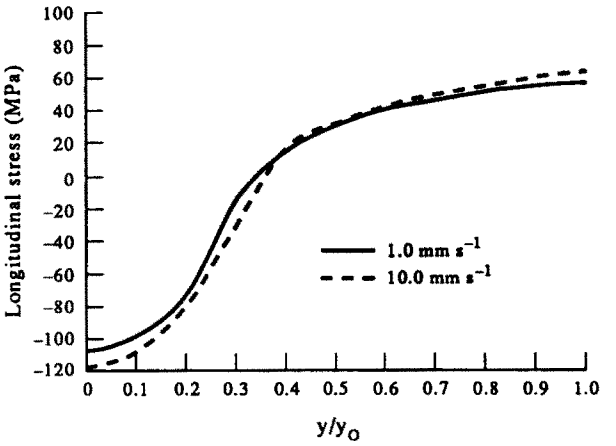

Fig. 19. Residual stress distributions over a cross section in plane-strain rollup as functions of roll velocity (—— 1.0 mm s^{-1}; – – – 10.0 mm s^{-1}).

10 mm s^{-1}, the residual stress peaks change from +55.0 to +61.6 MPa at the top and bottom faces and from −106.7 to −118.32 MPa at the center. Also, the residual stresses should be self-equilibrating. The distributions in Fig. 19 satisfy equilibrium with errors of less than 10%.

3.4. *Axisymmetric ring compression*

As in plane-strain slab rolling, a neutral region also exists in axisymmetric ring compression problems (see Fig. 20). This must be incorporated in the interface model.

3.4.1. *Interface modeling.* The interface conditions for axisymmetric upsetting can be best explained in terms of a local axisymmetric coordinate system (α, β, γ). The origin of this coordinate system is positioned at the tool–workpiece interface. For axisymmetric upsetting, let the α-axis be the tangential direction to the interface and let the β-axis be the outward normal (from the workpiece) at the interface. Here, γ denotes the hoop direction, and the γ-direction is identical to the global θ-direction. Hence, Cauchy traction rates at the interface can be expressed as

$$\tau_{\alpha}^{(c)} = \overset{\square}{\sigma}_{\alpha\beta} \tag{76a}$$

and

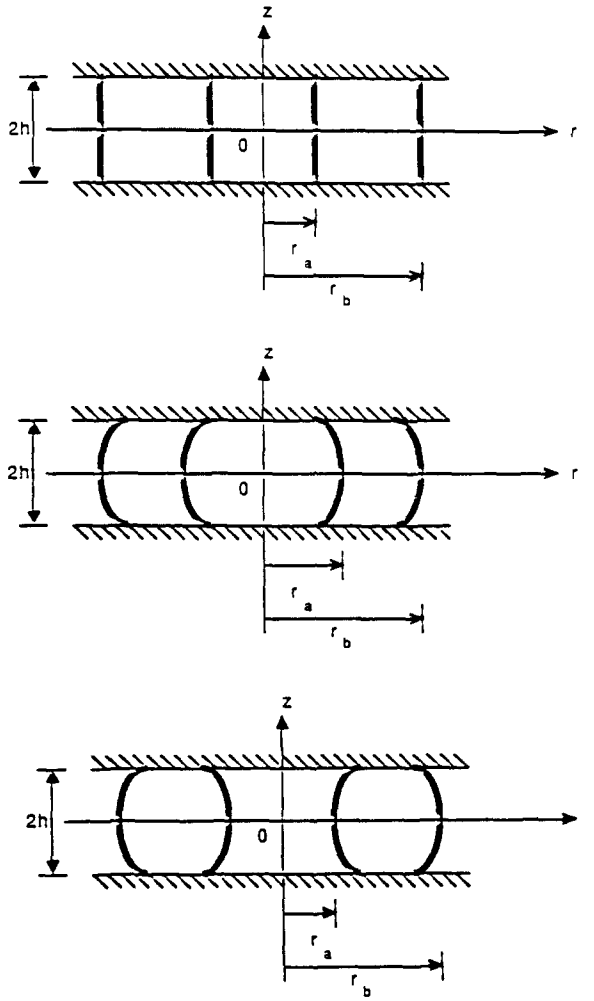

Fig. 20. Schematic diagram of ring compression: (a) undeformed shape; (b) first deformation mode; (c) second deformation mode.

$$\tau_{\beta}^{(c)} = \overset{\square}{\sigma}_{\beta\beta}. \tag{76b}$$

An axisymmetric version of the friction model of Chen and Kobayashi (1978) shown in eqn (74) is used to model the sliding contact at the tool–workpiece interface.

3.4.2. *Numerical results.* The particular material model used here is that due to Anand (1982). The particular material parameters used here are for Fe–0.05 carbon steel in a temperature range of 1173–1573 K and a strain rate range of 1.4×10^{-4} s^{-1} to 2.3×10^{-2} s^{-1}. Once again, for the sake of brevity, discussions on the material model are avoided here. Details of the material model along with the particular values of material parameters are given by Anand (1982) and Rajiyah and Mukherjee (1987).

The FEM calculations are carried out using the algorithm of Bathe and Chaudhary (1985) incorporated in the finite element analysis code ADINA. A similar strategy for FEM analysis has also been used by Carter and Lee (1986). An elastic–plastic material model (with isotropic work hardening) depicting the elastic–viscoplastic response of Fe–0.05 carbon steel in a temperature range of 1173–1573 K and at a strain rate of 10^{-3} s^{-1} is used in the FEM calculations. For the BEM analysis, the parameters for Anand's model were chosen to fit the response of the elastic–plastic model undergoing a tension test at a strain rate of 10^{-3} s^{-1}.

The ring geometry is chosen with a height-to-inner diameter-to-outer diameter ratio ($h : d_i d_o$) of 2 : 3 : 6. The diameter-to-height ratios ($d : h$) for the solid cylindrical specimens are 1.0, 2.0 and 3.0.

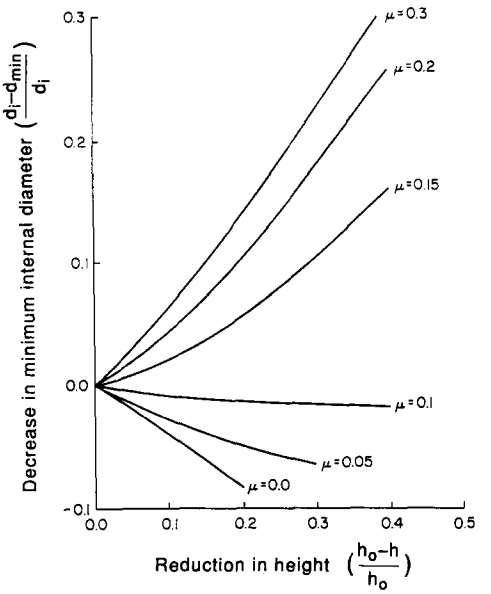

Fig. 21. Ring compression test calibration curves for different friction coefficients.

Figure 21 shows the changes in minimum internal diameter as functions of reduction in height during ring compression tests with different friction conditions at the interface. During a single ring compression test, the coefficient of friction is assumed to be constant spatially and temporally. When there is no friction at the interface and the workpiece can slide freely, the inner diameter, as well as the outer diameter, expands without bulging as the ring is compressed. For $\mu = 0.05$, both the inner periphery and the outer periphery bulge outward from the axis. For $\mu = 0.1$, however, the expansion of the inner diameter increases by only 2%. With further increases in the coefficient of friction, the deformed shape of the ring changes drastically. At $\mu = 0.15$, the inner periphery bulges inward while the outer periphery bulges outward, indicating the existence of a "neutral plane" in between. At a 40% reduction in height, the internal diameter reduces by 16%. The inward bulging of the inner surface becomes more pronounced with further increases in the friction coefficient. A similar trend is also observed by Chen and Kobayashi (1978) and Carter and Lee (1986).

Figure 22 shows the variation in pressure distributions at the interface at different stages of deformation. At a 10% reduction in height, the pressure distribution is almost uniform, with a slight increase at the outer periphery. With further deformation, the die pressure at a distance of about one-third of $(d_o - d_i)$ from the inner periphery also increases,

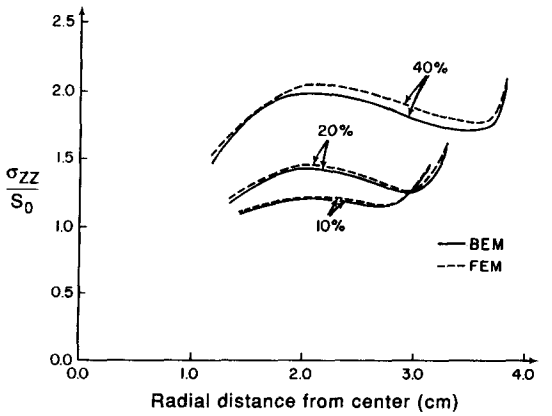

Fig. 22. Pressure distribution along the interface during ring compression test at different reductions in height ($\mu = 0.2$).

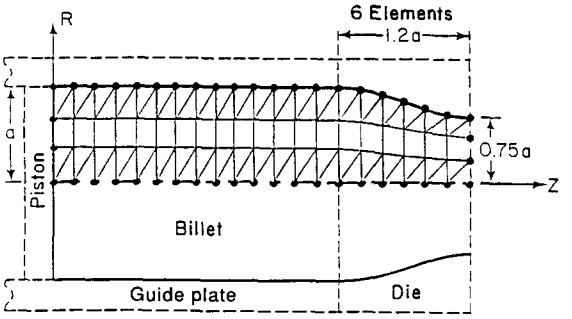

Fig. 23. Geometry of the axisymmetric extrusion problem.

and for a 40% reduction in height, shows a peak value of 1.98 for σ_{ZZ}/S_0 in this region. The pressure distributions at various stages of deformation obtained from the FEM analysis match quite well with those obtained from the BEM analysis. The maximum discrepancy in σ_{ZZ}/S_0 is less than 7%.

3.5. *Axisymmetric extrusion*

Many common extrusions and strip-drawing processes are axisymmetric in nature. The application of the BEM to analyse axisymmetric extrusion processes is discussed in this section. Particular attention is paid to die–workpiece interface conditions.

3.5.1. *Interface modeling.* Figure 23 is a schematic diagram of an axisymmetric extrusion process. The interface conditions for axisymmetric extrusion can be best explained in terms of a local coordinate system (α, β, γ). The origin of this coordinate system is positioned on the die–workpiece interface. The α-axis is tangential to the die surface, and the β-axis is the outward normal to the die surface. Here, γ represents the hoop direction and is identical to the global θ-direction. Hence, Cauchy traction rates at the interface can, once again, be expressed as

$$\tau_\alpha^{(c)} = \overset{\square}{\sigma}_{\alpha\beta} \tag{77a}$$

and

$$\tau_\beta^{(c)} = \overset{\square}{\sigma}_{\beta\beta}, \tag{77b}$$

in the local coordinate system. Cauchy traction rates can then be related to the Lagrange traction rates.

It is further assumed that the contact or lubricant layer adjacent to the die surface has zero stiffness in the direction tangential to the contact surface. Therefore, only pressures and shear loadings get transferred across the interface. Hence, $\sigma_{\alpha\alpha} = 0$ at the interface. Using the fact that the normal has components (0, 1, 0) in the local coordinate system, the Lagrange traction rates in the local coordinate system at the interface can be written as

$$\tau_\alpha^{(L)} = \overset{\square}{\sigma}_{\alpha\beta} - \sigma_{\beta\beta}\omega_{\beta\alpha} - \sigma_{\beta\alpha}d_{\beta\beta} + \sigma_{\beta\alpha}d \tag{78a}$$

and

$$\tau_\beta^{(L)} = \overset{\square}{\sigma}_{\beta\beta} - \sigma_{\beta\beta}d_{\beta\beta} - \sigma_{\beta\alpha}(d_{\beta\alpha} - \omega_{\beta\alpha}) + \sigma_{\beta\beta}d. \tag{78b}$$

It is assumed that sliding occurs in the $\alpha\beta$ plane only. A friction model of the type

$$\overset{\square}{\sigma}_{\alpha\beta} = \frac{G_s}{h} \cdot \mu v_\alpha, \tag{79a}$$

(Chandra and Mukherjee, 1987) is considered in the present analysis. Here, G_s and h are the shear modulus and height of the interface element, respectively, and μ represents the coefficient of friction. It is also assumed that $\sigma_{\alpha\beta}$ saturates to a value of $\mu\sigma_{\beta\beta}$. Thus,

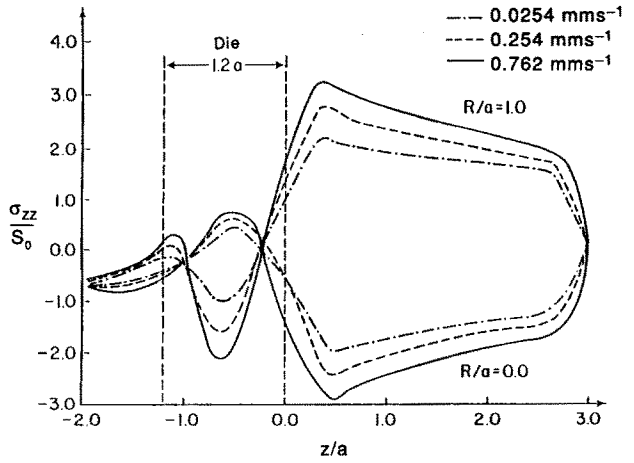

Fig. 24. Steady-state distribution of σ_{ZZ} at different piston velocities for two values of R ($\mu = 0$).

$$\overset{\square}{\sigma}_{\alpha\beta} = \frac{G_s}{h} \cdot \mu v_\alpha \quad \text{if } \sigma_{\alpha\beta} < \mu\sigma_{\beta\beta} \tag{79b}$$

and

$$\overset{\square}{\sigma}_{\alpha\beta} = 0 \qquad \text{if } \sigma_{\alpha\beta} = \mu\sigma_{\beta\beta}. \tag{79c}$$

Such an assumption is consistent with Coulomb's law of friction.

3.5.2. *Numerical results.* The material model used to analyse axisymmetric extrusion is that due to Anand (1982). The particular material parameters used here are for Fe–0.05 carbon steel in a temperature range of 1173–1573 K and strain rate range of $1.4 \times 10^{-4}\ s^{-1}$ to $2.3 \times 10^{-2}\ s^{-1}$. Details of the material model along with the particular values of material parameters are given by Anand (1982) and Rajiyah and Mukherjee (1987). For the friction model, the parameters $G_s/h = 1.268 \times 10^5$ MPa m^{-1}.

The FEM analysis reported here uses a piecewise quadratic description of velocities over triangular elements. Time integration for both the BEM and FEM programs are carried out by an explicit Euler-type method with automatic step control.

The geometry of axisymmetric extrusion considered here is shown in Fig. 23, and the numerical results are presented in Figs 24–27. Figure 24 shows the steady-state distributions of normalized axial stress, σ_{ZZ}/S_0, for three different piston velocities in the absence of friction, where S_0 is a material constant. In particular, the axis of the workpiece is chosen to be the z-axis and the stress distributions are shown for material points in the deformed configuration, which initially had the same relative radial position ($R/a = 0$ and $R/a = 1$)

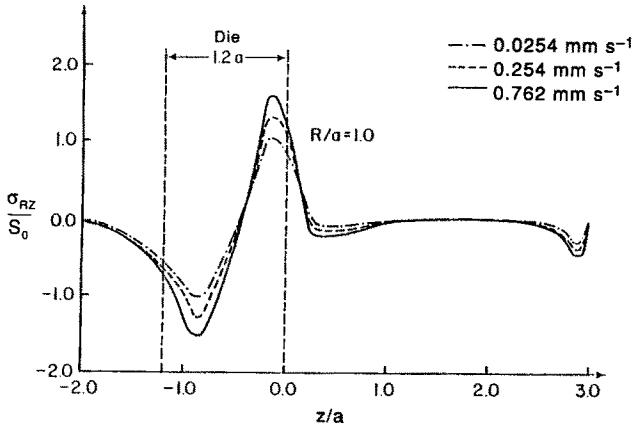

Fig. 25. Steady-state distribution of σ_{RZ} as functions of piston velocity ($\mu = 0.0$).

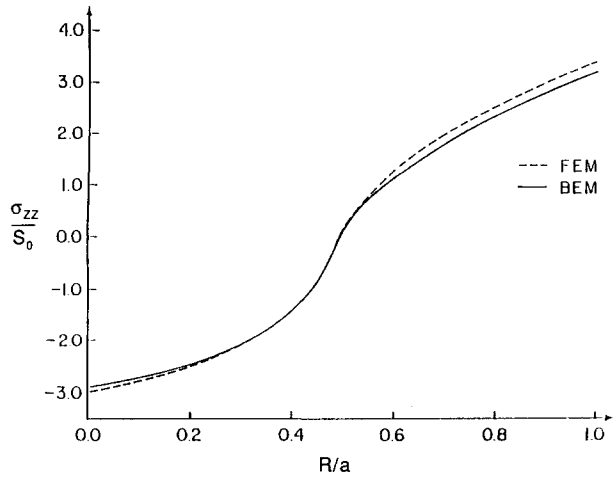

Fig. 26. Residual stress distribution across a transverse section (piston velocity = 0.762 mm s^{-1}, $\mu = 0.0$).

in the billet. Maximum residual tensile stress in an extruded workpiece is of crucial importance in design since this is the primary potential source for crack initiation and growth. It is seen from Fig. 23 that the rate dependence of σ_{ZZ}/S_0 is quite significant. As the piston velocity is tripled from 0.254 mm s^{-1} to 0.762 mm s^{-1}, the BEM analysis predicts a change of 17.75% in the maximum axial tensile stress in the workpiece. The faster the billet is forced through the die, the less time there is for stresses to relax at material points in the workpiece as they move through the die. Consequently, the maximum axial tensile stress upon exit from the die increases substantially with the speed of extrusion.

Another important feature of elastic viscoplastic analysis is that following a peak value, the magnitude of σ_{ZZ} decreases as a function of z in most of the billet that has passed through the die. This is a result of stress relaxation in the workpiece after it is deformed.

The results for the steady-state distributions of the shearing stress σ_{RZ} are shown in Fig. 25. It is shown that there is a significant variation of shearing stress in the die region. Residual axial stress distribution over a cross section at $z = 0.375a$ from the die exit are shown in Fig. 26. It should be noted that these residual stress distributions must be self-equilibrating and, for the residual stresses obtained from the current BEM analysis, the error in satisfying equilibrium is about 8% for σ_{ZZ} at $z = 0.375a$ from the die exit. At the die exit, the equilibrium of the residual σ_{ZZ} is satisfied with a 4% error and, at $z = 2a$, the error in equilibrium drops to less than 1%.

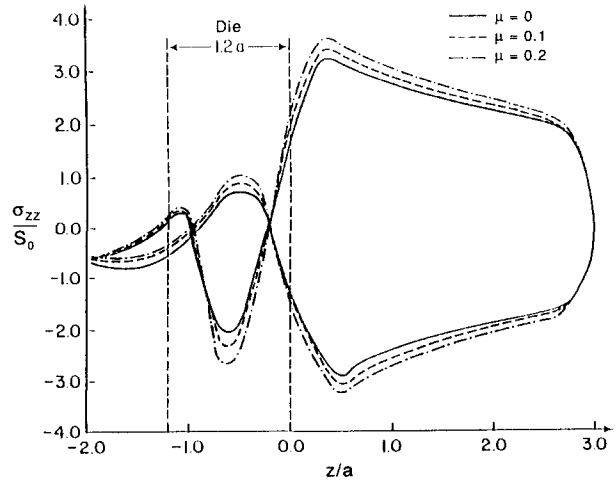

Fig. 27. Steady-state distribution of σ_{ZZ} as functions of friction coefficients for two values of R (piston velocity = 0.762 mm s^{-1}).

For comparison, the finite element code NIKE2D (Hallquist, 1986) is used for analysing the axisymmetric extrusion problem with no friction. NIKE2D cannot handle the state variable material model of Anand (1982). Accordingly, the stress–strain curve for a tension test at a strain rate of 0.5×10^{-2} s^{-1} is provided as the input material model to NIKE2D. The residual σ_{ZZ} at $z = 0.375$ obtained from NIKE2D is also shown in Fig. 25. The distributions obtained from the BEM analysis compare well with those obtained from the FEM analysis.

Figure 27 shows the effects of friction at the die–workpiece interface on the axial stress. Three different values of friction coefficients are chosen for a piston velocity of 0.762 mm s^{-1}. The presence of friction increases the peak value of the axial stress. Increasing the friction coefficient from $\mu = 0.0$ to $\mu = 0.2$ raises the peak value of σ_{ZZ}/S_0 from 3.25 to 3.63. The spatial position of the peak remains almost unchanged. It should be noted here that the friction model with constant coefficient of friction, as used in the present analysis, is crude at best. Much work remains to be done on accurate and realistic modeling of friction in metal forming processes. The present analysis does show, however, the qualitative effects that friction may have in the metal extrusion processes.

4. CONCLUSIONS

Forming is a widely used manufacturing process. The forming processes involve large strains and rotations, in addition to the material nonlinearities due to elastoplasticity and elastoviscoplasticity. The boundary conditions at the tool–workpiece interfaces are also complicated for forming processes.

Traditionally, FEM has been used to analyse metal forming problems. However, mesh degradation and inaccuracy of secondary variables are two common problems with such approaches.

The BEM is another general purpose method. This paper reviews the applications of the BEM for analysing several planar and axisymmetric metal forming problems. The BEM is far more tolerant of aspect ratio degradation than FEM and can deliver secondary variables that are as accurate as the primary ones. Handling of the interface friction conditions is also relatively easy through the load correction term in the BEM.

Further research is, of course, needed to verify the advantages BEM can offer for this class of problems. For axisymmetric problems, the BEM kernels are complicated elliptic functions. The kernel evaluations over internal cells are also very complicated and need care. Accordingly, the BEM axisymmetric calculations become inefficient if stress rates are evaluated at a large number of internal points. In most metal forming problems, however, the stresses on the boundary are of primary interest and, accordingly, a small number of internal points can be used.

The biggest advantage of BEM, however, lies in the reduction of the dimension of the problem by one, and this advantage becomes more and more significant as the size of the problems and the number of unknown variables increase. Recently, Zucchini and Mukherjee (1991) also observed that the BEM analyses can be parallelized very efficiently. For linear elastic problems, a speed-up of greater than five is reported on a six-processor machine (IBM 3090).

The particular problems analysed here are, of course, much simpler than real-life metal forming processes. However, the results provide crucial insights into various forming processes and establish the viability of the BEM for analysing such problems. Research is currently underway to refine the BEM methodology and to apply it to real-life metal forming problems.

Acknowledgements—Most of the research reported here is supported by Grant No. DMC 8657345 of the U.S. National Science Foundation to The University of Arizona. This financial support is gratefully acknowledged.

REFERENCES

Aifantis, E. C. (1984). On the microstructural origin of certain inelastic models. *ASME, J. Engng Mater. Tech.* **106**, 326–330.

Alexander, J. M. (1972). On the theory of rolling. *Proc. R. Soc. (London), Series A* **326,** 535–563.
Alexopoulos, P. S. (1981). An experimental investigation of transient deformation based on a state variable approach. Ph.D. thesis, Department of Material Science and Engineering, Cornell University, Ithaca, New York.
Anand, L. (1982). Constitutive equations for the rate dependent deformation of metals. *ASME, J. Engng Mater. Tech.* **104,** 12–17.
Atluri, S. N. (1984). On constitutive relations at finite strain: hypoelasticity and elastoplasticity and isotropic or kinematic hardening. *Comp. Meth. Appl. Mech. Engng* **43,** 137–171.
Avitzur, B. (1969). Bulge in hollow disk forging, Tech. Rept. AFML-TR-70-19.
Avitzur, B. (1980). *Metal Forming: The Applications of Limit Analysis.* Marcel Dekkar, New York.
Banerjee, P. K. and Butterfield, R. (1981). *Boundary Element Methods in Engineering Science.* McGraw-Hill, U.K.
Banerjee, P. K. and Cathie, D. N. (1980). A direct formulation and numerical implementation of the boundary element method for two-dimensional problems of elasto-plasticity. *Int. J. Mech. Sci.* **22,** 233–345.
Bardes, B. P. (Ed.) (1978). *Metals Handbook*, Vol. 1, ASM. Metals Park, Ohio.
Bathe, K. J. and Chaudhary, A. (1985). A solution method for planar and axisymmetric contact problems. *Int. J. Numer. Meth. Engng* **21,** 65–88.
Bhargava, V., Hahn, G. T. and Rubin, C. A. (1985). An elastic–plastic finite element model of rolling contact: (1) analysis of single contacts; (2) analysis of repeated contacts. *ASME, J. Appl. Mech.* **52,** 67–82.
Bui, H. D. (1978). Some remarks about the formulation of three-dimensional thermoelastic problems by integral equations. *Int. J. Solids Structures* **14,** 935–939.
Campos, L. T., Oden, J. T. and Kikuchi, N. (1982). A numerical analysis of a class of contact problems with friction in elastostatics. *Comp. Meth. Appl. Mech. Engng* **34,** 821–845.
Carter, W. T., Jr and Lee, D. (1986). Further analysis of axisymmetric upsetting, ASME, *J. Engng Ind.* **108,** 193–204.
Chandra, A. (1986). A generalized finite element analysis of sheet metal forming with an elastic–viscoplastic material model. *ASME, J. Engng Ind.* **108,** 9–15.
Chandra, A. (1989). Simulation of rolling processes by the boundary element method. *Comput. Mech.* **4,** 443–451.
Chandra, A. and Mukherjee, S. (1983). Applications of the boundary element method to large strain–large deformation problems of viscoplasticity. *J. Strain Anal.* **8,** 261–270.
Chandra, A. and Mukherjee, S. (1984a). Boundary element formulations for large strain–large deformation problems of viscoplasticity. *Int. J. Solids Structures* **20,** 41–53.
Chandra, A. and Mukherjee, S. (1984b). A finite element analysis of metal forming problems with an elastic–viscoplastic material model. *Int. J. Numer. Meth. Engng* **20,** 1613–1628.
Chandra, A. and Mukherjee, S. (1984c). A finite element analysis of metal forming processes with thermo-mechanical coupling. *Int. J. Mech. Sci.* **26,** 661–676.
Chandra, A. and Mukherjee, S. (1985). A boundary element formulation for sheet metal forming. *Appl. Math. Model* **9,** 175–182.
Chandra, A. and Mukherjee, S. (1986a). An analysis of large strain viscoplasticity problems including the effects of induced material anisotropy. *ASME, J. Appl. Mech.* **53,** 77–82.
Chandra, A. and Mukherjee, S. (1986b). A boundary element formulation for large strain problems of compressible plasticity. *Int. J. Engng Anal.* **3,** 71–78.
Chandra, A. and Mukherjee, S. (1987). A boundary element analysis of metal extrusion processes. *ASME, J. Appl. Mech.* **54,** 335–340.
Chandra, A. and Saigal, S. (1991). A boundary element analysis of the axisymmetric extrusion processes. *Int. J. Non-Lin. Mech.* **26,** 1–13.
Chandra, A. and Srivastava, R. (1991). A boundary element formulation for design sensitivities in problems involving both geometric and material nonlinearities. *Math. Comp. Model.* **15,** 81–92.
Chaudonneret, M. (1977). Methode des equations integrales appliquèes á la resolution de probléme de visco-plasticite. *J. de Mècanique Appliquè* **1,** 113–132.
Chaudonneret, M (1980). Structure computation in viscoplasticity; application to two-dimensional calculation of stress concentration. *Addendum to Proc. for the Second Int. Symp. on Innovative Numerical Analysis in Applied Engineering Science.* Montreal, Canada.
Chen, C. C. and Kobayashi, S. (1978). Rigid plastic finite element analysis of ring compression. *ASME, Appl. Numer. Meth. Forming Processes*, **AMD-28,** 163–174.
Cruse, T. A. (1969). Numerical solutions to three dimensional elastostatics. *Int. J. Solids Structures* **5,** 1259–1274.
Cruse, T. A. (1974). An improved boundary-integral equation method for three-dimensional elastic stress analysis. *Comput. Struct.* **4,** 741–754.
Dafalias, Y. F. (1984). A missing link in the formulation and numerical implementation of finite transformation elastoplasticity. In *Constitutive Equations: Macro and Computational Aspects* (Edited by K. J. William), pp. 25–40, ASME, New York.
Dawson, P. R. (1984). A model for the hot or warm forming of metals with special use of deformation mechanism maps. *Int. J. Mech. Sci.* **26,** 227–244.
Dawson, P. R. (1987). On modelling mechanical property changes during flat rolling of aluminum. *Int. J. Solids Structures* **23,** 947–968.
Dawson, P. R. and Thompson, E. G. (1977). Steady state thermomechanical finite element analysis of elasto-viscoplastic metal forming processes. *Numerical Methods for Manufacturing Processes*, pp. 167–182, ASME, New York.
Dienes, J. K. (1979). On the analysis of rotation and stress rate in deforming bodies. *Acta Mechanica* **32,** 217–232.
Doblare, M., Telles, J. C. F., Brebbia, C. A. and Alarcon, E. (1982). Boundary element formulation for elastoplastic analysis of axisymmetric bodies. *Appl. Math. Model* **6,** 130–135.
Eggert, G. M. and Dawson, P. R. (1987). On the use of internal variable constitutive equations in transient forming processes. *Int. J. Mech. Sci.* **29,** 95–113.

Goddard, J. D. and Miller, C. (1966). An inverse of the Jaumann derivative and some applications in the rheology of viscoelastic fluids. *Rheologica Acta* **5,** 177–184.

Hallquist, J. O. (1986). *NIKE2D—A Vectorized Implicit Finite Deformation Finite Element Code for Analyzing the Static and Dynamic Response of 2-D Solids with Interactive Rezoning and Graphics.* Lawrence Livermore National Laboratory, Livermore, CA.

Hart, E. W. (1976). Constitutive relations for the non-elastic deformation of metals. *ASME, J. Engng Mater. Tech.* **98,** 193–202.

Hart, E. W. (1982). The effects of material rotations in tension–torsion testing. *Int. J. Solids Structures* **18,** 1031–1042.

Hill, R. (1959). Some basic principles in the mechanics of solids without natural time. *J. Mech. Phys. Solids* **7,** 209–225.

Huang, Q.-P. and Du, Q.-H. (1988). An improved formulation for domain stress evaluation by boundary element methods in elastoplastic problems. In *China–U.S. Seminar on Boundary Integral Equations and Finite Elements Methods in Physics and Engineering.* Xian, People's Republic of China.

Jaswon, M. A. and Maiti, M. (1968). An integral equation formulation of plate bending problems. *J. Engng Math.* **2,** 83–93.

Jaswon, M. A. and Ponter, A. R. (1963). An integral equation solution of the torsion problem. *Proc. R. Soc. (London), Series A* **273,** 237–246.

Johnson, G. C. and Bamman, D. J. (1984). A discussion of stress rates in finite deformation problems. *Int. J. Solids Structures* **20,** 725–737.

Kármán, T. von (1925). On the theory of rolling. *Z. Angew. Math. Mech.* **5,** 130–141.

Kobayashi, S., Oh, S.-I. and Altan, T. (1989). *Metal Forming and the Finite Element Method.* Oxford University Press, New York.

Kumar, V., Morjaria, M. and Mukherjee, S. (1980). Numerical integration of some stiff constitutive models of inelastic deformation. *ASME, J. Engng Mat. Tech.* **102,** 92–96.

Lange, K. and Kurz, N. (1984). *Theoretical and Experimental Investigations of the 'Grob' Cold Shape-Rolling Process.* Inst. Metal Forming, University of Stuttgart, West Germany.

Lee, C. H. and Altan, T. (1972). Influence of flow stress and friction upon metal flow in upset forging of rings and cylinders. *J. Engng Ind.* **94,** 1149–1155.

Lee, E. H., Mallet, R. L. and Yang, W. H. (1977). Stress and deformation analysis of metal extrusion processes. *Comput. Meth. Appl. Mech. Engng* **10,** 339–353.

Li, G. J. and Kobayashi, S. (1982). Rigid–plastic finite element analysis of plane strain rolling. *ASME, J. Engng Ind.* **104,** 55–64.

Martins, J. A. C. and Oden, J. T. (1983). A numerical analysis of a class of problems in elastodynamics with friction. *Comput. Meth. Appl. Mech. Engng* **40,** 327–360.

McMeeking, R. M. and Rice, J. R. (1975). Finite element formulation for problems of large elastic–plastic deformation. *Int. J. Solids Structures* **11,** 601–616.

Mendelson, A. (1973). Boundary integral methods in elasticity and plasticity, NASA TND-7418, NASA-Lewis Res. Center, Cleveland, Ohio.

Merwin, J. E. and Johnson, K. L. (1963). An analysis of plastic deformation in rolling contact. *Proc. Inst. Mech. Engng* **177,** 667–673.

Mori, K., Osakada, K. and Oda, T. (1982). Simulation of plane-strain rolling by the rigid–plastic finite element method. *Int. J. Mech. Sci.* **24,** 519–527.

Mukherjee, S. (1982). *Boundary Element Methods in Creep and Fracture.* Elsevier Applied Science Publishers, Barking, Essex, U.K.

Mukherjee, S. and Chandra, A. (1984). Boundary element formulations for large-strain–large deformation problems of plasticity and viscoplasticity. In *Developments in Boundary Element Methods* (Edited by P. K. Banerjee and S. Mukherjee), Vol. 3, Chapter 2, pp. 27–58, Elsevier Applied Science Publishers, Barking, Essex, U.K.

Mukherjee, S. and Chandra A. (1987). Nonlinear solid mechanics. In *Boundary Element Methods in Mechanics* (Edited by D. E. Beskos), pp. 285–331. North-Holland Publishers, Amsterdam.

Nemat-Nasser, S. (1982). On finite deformation elasto-plasticity, *Int. J. Solids Structures* **18,** 857–872.

Oh, S. I. Park, J. J., Kobayashi, S. and Altan, T. (1983). Application of FEM modelling to simulate metal flow in forging a titanium alloy engine disk. *ASME, J. Engng Ind.* **105,** 251–258.

Okada, H., Rajiyah, H. and Atluri, S. N. (1987). Non-hyper-singular-integral representation for velocity (displacement) gradients in elastic/plastic solids (small or finite deformations). Georgia Institute of Technology, Atlanta, GA.

Onate, E. and Zienkiewicz, O. C. (1983). A viscous shell formulation for the analysis of thin sheet metal forming. *Int. J. Mech. Sci.* **25,** 305–335.

Orowan, E. (1943). The calculation of roll pressure in hot and cold flat rolling. *Proc. Inst. Mech. Engng* **150,** 140–167.

Pires, E. B. and Oden, J. T. (1983). Analysis of contact problems with friction under oscillating loads. *Comp. Meth. Appl. Mech. Engng* **39,** 337–362.

Rajiyah, H. and Mukherjee, S. (1987). Boundary element analysis of inelastic axisymmetric problems with large strains and rotations. *Int. J. Solids Structures* **23,** 1679–1698.

Riccardella, P. (1973). An implementation of the boundary integral technique for plane problems of elasticity and elasto-plasticity. Ph.D. thesis, Carnegie Mellon University, Pittsburgh, Pennsylvania.

Rizzo, F. J. (1967). An integral equation approach to boundary value problems of classical elastostatics. *Q. Appl. Math.* **25,** 83–95.

Rizzo, F. J. and Shippy, D. J. (1968). A formulation and solution procedure for the general nonhomogeneous elastic inclusion problems. *Int. J. Solids Structures* **4,** 1161–1179.

Rolph, W. D. and Bathe, K. J. (1984). On a large strain finite element formulation for elasto-plastic analysis. In *Constitutive Equations: Macro and Computational Aspects* (Edited by K. J. William), pp. 131–147, ASME, New York.

Swedlow, J. L. and Cruse, T. A. (1971). Formulation of boundary integral equations for three-dimensional elasto-plastic flow. *Int. J. Solids Structures* **7,** 1673–1681.

Telles, J. C. F. and Brebbia, C. A. (1983). Viscoplasticity and creep using boundary elements. In *Progress in Boundary Element Methods*, Vol. 2 (Edited by C. A. Brebbia), pp. 200–215, Pentech Press, London.

Torstenfelt, B. (1983). Contact problems with friction in general purpose finite element computer programs. *Comput. Struct.* **16,** 487–493.

William, K. J. (Ed.) (1984). *Constitutive Equations: Macro and Computational Aspects.* ASME, New York.

Zolti, E. (1983). A finite element procedure to time dependent contact analysis. *Comput. Struct.* **17,** 555–561.

Zucchini, A. and Mukherjee, S. (1991). Vectorial and parallel processing in stress analysis with the boundary element method (private communication).